

GENERATION OF TUNABLE BROADBAND
DEEP ULTRAVIOLET RADIATION FROM GASEOUS
MEDIA USING ULTRASHORT LASER PULSES.

Master Thesis

by Esben Witting Larsen
Aarhus, July 2011



Department of Physics and Astronomy
Aarhus University



Department of Physics
Lund University

GENERATION OF TUNABLE BROADBAND DEEP ULTRAVIOLET RADIATION
FROM GASEOUS MEDIA USING ULTRASHORT LASER PULSES.

© 2011 Esben Witting Larsen

Faculty of Science
Department of Physics and Astronomy
Aarhus University
Ny Munkegade 120
8000 Aarhus C
Denmark

<http://phys.au.dk/>

Division of Atomic Physics
Department of Physics
Faculty of Engineering, LTH
Lund University
P.O. Box 118
221 00 Lund
Sweden

<http://www.atomic.physics.lu.se>

English abstract

Most modern ultrafast lasers are based on mode-locked fiber or solid-state lasers and operate around the near infrared part of the electromagnetic spectrum. The widely spread CPA based Titanium Sapphire lasers can emit pulses centred around 800 nm with durations down to 20 fs. However, for many ultrafast experiments light at different centre frequencies are required. In order to obtain other centre frequencies, nonlinear optical processes are employed.

The conventional way of frequency conversion is to use nonlinear crystals, which generally offers ways of generating ultrashort ranging from the near-infrared to the near-ultraviolet. At shorter wavelengths this technique is limited due to strong dispersion of the existing nonlinear crystals. Ultrashort extreme ultraviolet light can be generated through the process of high harmonic generation. However, a gap in available ultrashort pulses with centre frequencies exists in the intermediate deep ultraviolet ($\lambda < 300$ nm) and vacuum ultraviolet ($\lambda < 200$ nm) regions.

This Master Thesis, which was performed in Sweden at Lund High-Power Laser Facility, aimed to close the gap with main focus on the deep ultraviolet regions. The generation of ultrashort deep ultraviolet was studied both experimentally and theoretically. A particular focus of the project was to keep the experimental relatively simple without the use of highly sophisticated vacuum installations, nor complicated pulse re-compressions schemes. To avoid limitations caused by dispersion only gaseous interaction media was considered.

Different experimental four-wave mixing schemes for nonlinear frequency conversion of the output from CEP stable 3 mJ, 1 kHz 30 fs Titanium Sapphire laser was studied. Direct third harmonic generation was experimentally investigated in a static gas cell, which was designed and realized in this project. The gas cell experiments were supported by numerical simulations of phase-matching conditions for third harmonic generation. Additionally was third harmonic generation experimentally studied in a pulsed gas jet, as well as in a gas filled hollow capillary.

Finally, was third harmonic frequency light experimentally realized by phase-matched difference frequency mixing between the fundamental frequency pulses from the laser, and frequency doubled pulses (generated in a KDP crystal), in a hollow capillary.

Direct third harmonic generation in the static pressure gas cell provided the most powerful deep ultraviolet pulses generated within this work. The pulsed gas jet provided slightly less output power. However, increased reproducibility and mode quality strongly outweighed the loss of power.

Phase-matched difference frequency generation in a hollow capillary, although experimentally the most demanding, yielded the most promising results. Deep ultraviolet pulses centred around 260 nm with estimated energies exceeding 1 μ J, and a spectral width of 50 nm was demonstrated at low pressures in the capillary. The bandwidth principally supports pulse durations down to 2 fs. The scheme also allowed for tunability of the output pulses; by changing the intensity of the fundamental field, the centre wavelength of the deep ultraviolet pulse could be tuned over 10 nm. Finally, at high pressures broadband light with spectral components covering the entire spectrum from 200-1100 nm was demonstrated.

Danish abstract

De fleste moderne ultrahurtige lasere er baseret på mode-locked fiber eller faststof-lasere og opererer i den nærinfrarøde del af det elektromagnetiske spektrum. De vidt udbredte CPA baserede titanium safir lasere kan leve lys pulser med centerbølgelængder omkring 800 nm og varigheder ned til 20 fs. De fleste ultrahurtige eksperimenter kræver imidlertid lys med andre center bølgelængder. For generere lys pulser med andre centerbølgelængder anvendes ikke-lineære optiske processorer.

Den konventionelle måde at foretage frekvenskonvertering er ved at bruge ikke-lineære krystaller. Denne metode kan generelt anvendes til at generere ultrakorte pulser lige fra det nær-infrarøde til nær-ultraviolet del af det elektromagnetiske spektrum. For kortere bølgelængder er teknikken med ikke-lineære krystaller begrænset grundet øget dispersion. Ultrakort ekstrem ultraviolet lys pulser kan genereres via processen kaldet høj harmonisk generation. Det er imidlertid ikke muligt at genererer ultrakorte pulse i de mellemliggende bølgelængder fra 100-300 nm.

I dette speciale, som blev udført i Sverige hos Lunds High-Power Laser Facility, havde til formål at lukke dette hul med hovedfokus på området fra 200-300 nm. Generation af ultrakort ultraviolet lys pulse med disse centerbølgelængder blev studeret både teoretisk og eksperimentelt. Et særligt fokus i projektet gik på at holde den eksperimentelle opstilling relativt simpel uden brug af meget avancerede vakuum installationer, eller komplicerede puls re-komprimerings foranstaltninger. For at undgå begrænsninger forårsaget af dispersion, blev udelukkende gaser betragtet som medium for den ikke-lineære vekselvirkning.

Der blev undersøgt flere ikke-lineære frekvenskonvertering metoder til at generer dybt ultraviolet lys udaf 800 nm, 3 mJ og 30 fs pulseret lys leveret af en CEP stabil titanium safir laser med en repetitionsfrekvens på 1 kHz. Direkte tredje harmonisk generation blev eksperimentelt undersøgt i en gas celle med et statisk tryk. Cellen blev både designet og bygget til dette projekt. Gas celle forsøgene blev støttet af numeriske simuleringer af fase-matchnings betingelserne for tredje harmonisk generation. Derudover blev tredje harmonisk generation eksperimentelt undersøgt i både en pulseret gas jet, og i et gasfyldt hult kapillarrør. Endelig blev lys med tre gange den fundamentale frekvens skabt ved hjælp af faseafstemt forskel frekvens blanding af lys med den fundamentale frekvens og den anden ordens harmoniske frekvens i et kapillarrør. Det anden ordens harmoniske felt blev genereret i en ikke-lineær krystal.

Direkte tredje harmonisk generation af lys i en gas celle med et statiske tryk, forsagede de mest kraftfulde ultraviolette pulser, som blev mlt i forbindelse med dette speciale. Den pulserende gas jet var i stand til at levere pulser med næsten samme styrke, men var så til gengæld i stand til at vedligeholde produktionen over længere tid.

Den faseafstemte forskel frekvens generation i det hule kapillarrør, som var den mest eksperimentelt krævende opstilling, gav imidlertid de mest lovende resultater. Ved lavt gas tryk i det kapillarrør var det muligt at skabe 1 μ J ultraviolette pulser med en centerbølgelængde på 260 nm og en spektral båndbredde på 50 nm. Så spektralt bredt lys er teoretisk set i stand til at understøtte ultrakorte pulser med varigheder ned til 2 fs. Derudover var det muligt at justere centerbølgelængden på det genererede UV lys med op til 10 nm blot ved at ændre intensiteten på det fundamentale felt. Endeligt var det muligt ved højt tryk i røret at producerer bredbåndsls, der dækkede hele spektret fra 200 - 1100 nm.

ABBREVIATIONS

AOPDF	Acousto Optic Programmable Dispersive Filter
BBO	Beta Barium Borate
CEP	Carrier Envelope Phase
CaF ₂	Calcium Fluoride
CPA	Chirped Pulse Amplification
CW	Continuous Wave
DFG	Difference Frequency Generation
FWHM	Full Width Half Maximum
GVD	Group Velocity Dispersion
HeNE	Helium Neon
IR	Infra-Red
KDP	Potassium Dihydrogen Phosphate
KD*P	Potassium Dideuterium Phosphate
LMS	Least Mean Square
PEEM	Photoemission Electron Microscopy
PPLN	Periodically Poled Lithium Niobate
SFG	Sum Frequency Generation
SHG	Second Harmonic Generation
SiO ₂	Silica
SPM	Self Phase Modulation
TEM	Transverse Electro Magnetic
THG	Third Harmonic Generation
Ti:Al ₂ O ₃	Titanium Doped Sapphire
UV	Ultraviolet
VUV	Vacuum Ultraviolet
XUV	Extreme Ultraviolet

CONTENTS

1	Introduction	1
1.1	The purpose of this Master Thesis	2
1.2	Outline of the thesis	3
2	Nonlinear optics	5
2.1	The basic nonlinear interactions	6
2.1.1	Phase matching in SHG	7
2.2	Nonlinear interaction with focused beams	8
2.3	Quantum mechanical description of the electric susceptibility	10
2.3.1	Nonlinear optics in isotropic materials	12
3	Phase matching and nonlinear induced refractive index shifts	15
3.1	Sellmeier equations	15
3.2	Group velocity and GVD	15
3.3	Refractive index corrections	17
3.3.1	Nonlinear refractive index	17
3.3.2	Plasma contribution to the refractive index	18
3.3.3	Modal dispersion in a waveguide	19
4	Numerical simulations	21
4.1	Estimation of the plasma density	22
4.2	Simulation of THG light	24
5	The experiment	29
5.1	Detailed description of the laser system	29
5.1.1	The oscillator	30
5.1.2	The stretcher	32
5.1.3	The pulse amplification	33
5.1.4	The compressor	33
5.1.5	Beamline for the setup	34
5.2	The vacuum system	34
5.2.1	The windows	35
5.2.2	Mechanical support	36
5.3	The static gas cell experiments	37
5.3.1	Results and discussions for the static gas cell	39
5.4	The pulsed gas jet experiments	42
5.4.1	Results and discussions	43
5.5	The hollow capillary experiments	44
5.5.1	The two-color interferometer	44
5.5.2	Aligning the hollow capillary	46
5.5.3	Results and discussions	46
6	Conclusions and outlook	53
6.1	Outlook	54
	Acknowledgements	57
	References	59

INTRODUCTION

For large parts of the history of optics, it was believed that the optical properties of materials were independent of the intensity of light. This is not the case; an intense light field fundamentally alters the optical response of materials. Nonlinear optics is the study of phenomena, which occur when the light is intense enough for this to happen. The phenomena are nonlinear in the sense that they occur when the optical response of the material stops acting linearly with respect to the strength of the applied optical field.

The first nonlinear optical process was demonstrated by Franken *et al.* merely one year after the invention of the first laser by Theodore Maiman in 1960[1, 2]. Franken observed how red light delivered by a ruby laser focused into a quartz crystal was converted into blue light. The so-called second harmonic generation (SHG) occurred because the early lasers were naturally pulsed with durations around 1 ms, so when focused, the beam was intense enough for nonlinear interactions to take place. Q-switching and mode-locking techniques soon followed and allowed for ways of controlling the pulsed operations of lasers, which marked the real start of nonlinear optics.

The shortest possible duration of an electromagnetic pulse is inversely proportional to its spectral bandwidth. So, while the early lasers were optimized for monochromaticity for precise spectroscopy studies in the frequency domain, an important branch in nowadays laser research focuses on the development of ultra-broadband laser radiation. By locking the various spectral component of broadband light in phase it is possible to generate optical pulses with durations in the attosecond (10^{-18} s) to femtosecond (10^{-15} s) range[3]. Such short pulses have allowed for spectroscopy to move to the temporal domain, with a temporal resolution comparable to the oscillation period of an electron orbiting an atom.

Lasers which are capable of delivering pulses with sub-picosecond durations are usually called ultrafast, while the pulses from such systems are called ultrashort. The majority of such lasers is either based on mode-locked fiber or solid state lasers, and operates in the infrared (IR) to near-infrared region of the electromagnetic spectrum. The most wide-spread system is probably the chirped pulse amplification based Ti:Sapphire laser with post-amplification pulse durations down to 20 fs.

For pulses with center frequencies ranging from the near ultraviolet to the near infrared, similar durations are usually generated by frequency up- or down-conversion of light delivered by such a system, through low-order harmonic generation, optical parametric processes, or sum- and difference frequency generation. Extreme

ultraviolet light (XUV) with sub-femtosecond durations are made accessible by the process of high harmonic generation[4–6]. Currently a gap in available ultrashort light pulses exists in the intermediate deep ultraviolet ($\lambda < 300$ nm, DUV) to vacuum ultraviolet ($\lambda < 200$ nm, VUV) regions. The aim of this thesis was to try to close this gap, with main focus on the DUV part.

Ultrashort DUV light will find applications in various pump-probe¹ temporal studies. In particular, either as a pump or a probe in time-resolved photoemission electron microscopy[7], a pump in ultrafast charge migration studies of large molecules[8], or as a pump in the investigation of movement of excited bound state electrons[9].

The presented work was mainly inspired by the generation of 2.8 fs (FWHM) third harmonic pulses from 4 fs long 750 nm light pulses presented in [10], and the generation of broadband frequency combs in the DUV and the VUV through cascaded third-order nonlinearities presented in [11].

1.1 The purpose of this Master Thesis

The normal way of generating ultrashort pulses in the near- to vacuum ultraviolet regimes by subsequent upconversion of the light in a number of crystals[12, 13] is limited by the effects of dispersion and absorption. Dispersion spreads the various frequencies of the pulse in time, so for ultrashort pulses which are also very broad band this leads to significantly increased pulse duration. In addition, the dispersive effects in most materials become increasingly strong for shorter wavelengths, so while the effect is small for second harmonic generation, it is not for further upconversion. Dispersion can to some extent be compensated for by temporal recompression of the light pulses. However, since the bandwidth of the nonlinear processes also depends on dispersion, the spectral bandwidth of the upconverted light is reduced within each crystal. The reduced bandwidth ultimately leads to longer minimal pulse duration.

The main purpose of this master thesis was therefore to investigate alternative methods of generating deep ultraviolet radiation from an ultrashort pulsed laser. By using a broadband short pulse in a weakly dispersive medium, such as a gas, the generated pulse naturally inherits the characteristics of the generating pulse without the need for temporal recompression afterwards. Additionally the idea was to achieve this by using a simple setup without the requirement of a sophisticated high-vacuum installation. Four different methods for generation of ultraviolet light were investigated.

- (i) Direct third harmonic generation in a static pressure gas cell.
- (ii) Direct third harmonic generation in a pulsed gas jet.
- (iii) Direct third harmonic generation in a hollow capillary.
- (iv) Phase matched low order harmonic generation inside a hollow capillary by the use of two-color laser fields.

¹In a typical pump-probe scheme two light pulses are used; the first pulse (pump) is used to prepare a system in a given state for investigation, while the second pulse (probe) is used to investigate this state.

1.2 Outline of the thesis

The report is divided into six chapters. The second chapter provides a formal introduction to nonlinear optics. The most fundamental nonlinear interactions involved in frequency conversion of light are described, concluded with a quantum mechanical description of the electric susceptibility. The third chapter deals with the aspect of phase matching. Descriptions of the origins of the various parameters, which can give rise to a change in the phase-matching condition, are given. In chapter four a simple model for simulation of third harmonic generation in a static gas cell is presented followed by a preliminary discussion about what to focus on for the experimental part. Chapter five presents the experimental setup and results from the various experiments conducted in this work. The final chapter summarizes the work presented within this thesis. The various methods of generation of deep ultraviolet light are evaluated, while the thesis is concluded with an outlook.

NONLINEAR OPTICS

The polarization P of a dielectric medium is defined as the dipole moment per unit volume[14]. When the medium is exposed to an external electric field, the nucleus and electrons constituting the medium, start to reorganize to the new conditions, resulting in the creation of microscopic atomic and molecular dipoles. We normally consider the polarization to be linear with the applied field. However, the discoveries by Franken and others in the early days of the laser showed that this is in fact not the case. The nonlinearity in the generation of dipoles can easily be understood in terms of the simple classical Lorentz model of the atom, where an electron is connected to the nucleus through a spring[15]. Hookes law states that if the spring-like electron-atom pair is subjected to a small external force the electron is displaced from the equilibrium position by a distance, which is proportional to the external force. However, Hookes law breaks down if the applied force becomes comparable to the spring force and the displacement stops being linear - we move into the nonlinear regime. In the simplest example of the hydrogen atom, the Coulomb potential at Bohr radius is roughly $5 \cdot 10^{11}$ V/m. Field strength of similar magnitudes is easily obtained with today's lasers.

The propagation of light is governed by the wave equation, which is derived from Maxwell's Equations. For a nonmagnetic¹ medium with nonlinear electric response in the absence of free currents, the wave equation takes the following form in the time domain[16]:

$$\nabla^2 E(\mathbf{r}, t) - \frac{1}{c^2} \frac{\partial^2}{\partial t^2} E(\mathbf{r}, t) = \mu_0 \frac{\partial^2}{\partial t^2} P(\mathbf{r}, t), \quad (2.1)$$

where E is the electric field, P the polarization, while c is the speed of light in vacuum and μ_0 the permeability of vacuum.

In the linear regime the polarization is linked to the electric field as: $P(t) = \epsilon_0 \chi^{(1)} E(t)$, where $\epsilon_0 = (\mu_0 c^2)^{-1}$ is the vacuum permittivity and $\chi^{(1)}$ is the linear susceptibility. The refractive index n is related to the susceptibility as: $n^2 = 1 + \chi^{(1)} = \frac{\epsilon}{\epsilon_0} \equiv \epsilon_r$. Finally the wavenumber is given by: $k = \frac{\omega}{c} \sqrt{\epsilon_r} = \frac{\omega}{c} n$.

In the case of nonlinear optics the polarization can be written as a power series

¹Throughout this report we assume that the materials are nonmagnetic.

of the electric field:

$$\begin{aligned}
 P_i(t) &= \epsilon_0 \left(\sum_j \chi_{ij}^{(1)} E_j(t) + \sum_{jk} \chi_{ijk}^{(2)} E_j(t) E_k(t) + \sum_{jkl} \chi_{ijkl}^{(3)} E_j(t) E_k(t) E_l(t) + \dots \right) \\
 &\equiv P_i^{(1)}(t) + P_i^{(2)}(t) + P_i^{(3)}(t) + \dots, \tag{2.2}
 \end{aligned}$$

where the sums are taken over the spatial coordinates. As apparent from the equation the different $\chi^{(k)}$ are tensors of rank $k + 1$, for completeness with the linear case they are usually called the k 'th order susceptibility, likewise are the $P_i^{(k)}$ referred to as the k 'th order polarizations. Although the polarization manifests itself in the time domain it is most readily solved in the frequency domain by performing a frequency decomposition of both the electric fields and the polarizations.

2.1 The basic nonlinear interactions

The simplest nonlinear process is the so-called Second Harmonic Generation of light (SHG). In SHG two photons with the same frequency are converted into a single photon with twice the frequency $\omega + \omega = 2\omega$. The process is due to the second order nonlinear polarization, higher order terms can likewise lead to higher order harmonic generation. As another example third order generation is due to the third order polarization and so forth.

Harmonic generation is just a special case of Sum Frequency Generation (SFG) between degenerate fields. As the name implies SFG is the event where a number of photons with the same or different frequencies ω_i are converted into a single photon with the sum frequency. As opposed to the sum frequency process we also have the most general of the simple interactions, namely the Difference Frequency Generation (DFG). In DFG the resulting photon can have any possible mixture of frequencies of the input photons, in the simple case of DFG of two photons with frequencies ω_1, ω_2 the possible frequencies for the generated photon is: $\omega_3 = \omega_1 - \omega_2$ and $\omega_3 = \omega_2 - \omega_1$. The final of the simple processes associated with all nonlinear terms of the polarization is the process known as optical rectification[17] where photons eliminate through DFG, causing a static electric field across the nonlinear medium. Optical rectification can be understood from DFG; as the elimination of a high frequency photon creating a photon with slightly lower frequency and a photon with very low frequency.

Returning to the SFG process in the case of two collinear beams² with intensities I_1, I_2 , the amount of light generated at ω_3 through the second order polarization in a lossless medium of length L in the undepleted pump and loose focusing approximations is given by³:

$$I_3 = \frac{(\chi^{(2)}\omega_3)^2}{2n_1n_2n_3\epsilon_0c^3} I_1 I_2 L^2 \text{sinc}^2 \left(\frac{\Delta k L}{2\pi} \right), \tag{2.3}$$

²For the remainder of this report, all beams are assumed to be collinear, unless otherwise specified.

³Chapter 2.2 of [16]. There is a small misprint in the final result given in (2.2.19) of the reference, however (2.2.17) is correct. Also the expression given here is for the normalized sinc function.

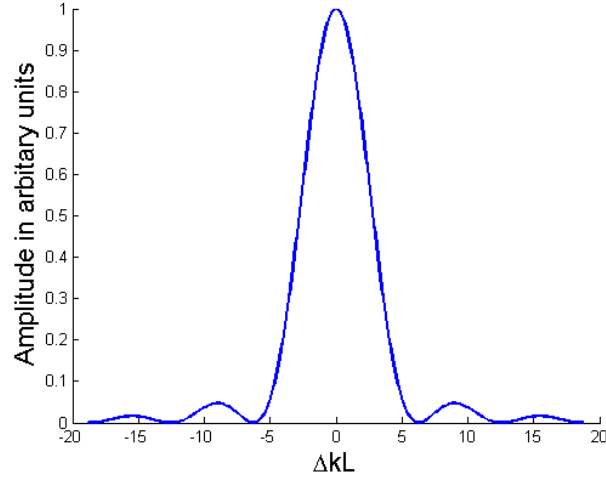


Figure 2.1: Effects of phase mismatch on the generated output.

where n_i are the refractive indices at the respective frequencies and Δk is the wavevector mismatch, which ensures momentum conservation, given by:

$$\Delta k = k_1 + k_2 - k_3. \quad (2.4)$$

The quantity ΔkL is called the phase mismatch, since it is a measurement of the phase difference between the input and output fields. From equation (2.3) it is seen that the generated output depends strongly on the phase mismatch through the $\text{sinc}^2\left(\frac{\Delta kL}{2\pi}\right)$ function, which has been plotted in figure 2.1. If $\Delta kL = 0$ the output is maximized and the process is therefore called phase-matched. The distance $L_{\text{coh}} = \frac{2\pi}{\Delta k}$ is sometimes referred to as the coherence length, since $\text{sinc}^2\left(\frac{\Delta kL}{2\pi}\right)$ vanishes at this length.

2.1.1 Phase matching in SHG

Returning to the special case of SHG in this case the wavevector mismatch is given by:

$$\Delta k = 2k(\omega) - k(2\omega) = 2\frac{\omega}{c}n(\omega) - \frac{2\omega}{c}n(2\omega). \quad (2.5)$$

In a normal dispersive medium⁴ phase matching is not possible for optical wavelengths, hence the generated signal is reduced. One solution is to use a birefringent material, such as quartz or more prominently BBO⁵ or KDP⁶ crystals. In a birefringent material the refractive index is dependent on the polarization of the light with respect to the optical axes of the crystal. A crystal with only one optical axis is called a uniaxial crystal, while crystals with two optical axes are called biaxial. In the case of beam propagation in an uniaxial crystal, light which is polarized perpendicular to the plane containing the propagation vector \mathbf{k} , and the optical axis \mathbf{o} is called ordinary polarized, while light polarized within this plane is called extraordinary polarized. The extraordinary polarized light experiences a refractive index

⁴See section 3.2.

⁵Beta Barium Borate

⁶Potassium Dihydrogen Phosphate

n_e , which is dependent on the angle θ between \mathbf{k} and \mathbf{o} according to[15]:

$$\frac{1}{n_e^2(\theta)} = \frac{\sin^2 \theta}{n_e^2(\theta = 0)} + \frac{\cos^2 \theta}{n_o^2}, \quad (2.6)$$

where n_o is the refractive index for ordinary polarized light, which as indicated by the name and the formulation of (2.6) does not dependent on θ . Phase matching is obtained by turning the crystal and thereby changing the extraordinary refractive index.

2.2 Nonlinear interaction with focused beams

It is apparent that the nonlinear response of a medium increases with stronger applied fields. One way of enhancing the nonlinearities is therefore to increase the intensity of the applied field; this can readily be done by focusing the beam. This section describes how the focusing of a beam affects the nonlinearity.

A paraxial beam⁷ propagating along the z -axis obeys the paraxial wave equation for the electric field envelope A_q , which in the case of nonlinear optics with a source term S_q takes the following form[16]:

$$2ik_q \frac{\partial A_q}{\partial z} + \nabla_T^2 A_q = -S_q e^{i\Delta k_q z}, \quad (2.7)$$

where S_q is a spatially varying source, and Δk_q represents a possible wavevector mismatch between the source and the applied field. A frequency decomposition of the electric field and source have been performed in deriving (2.7). The source free equation ($S_q = 0$) is solved by the Hermite-Gaussian profiles with the so-called Transverse Electro Magnetic modes abbreviated as TEM _{nm} . The lowest order Hermite-Gaussian is the TEM₀₀ and is given by:

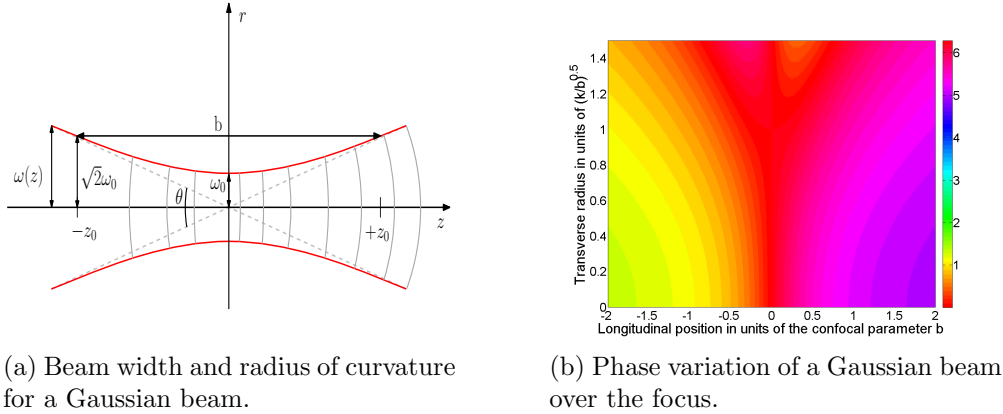
$$A(z, r) = \frac{a}{\sqrt{1 + \left(\frac{2z}{b}\right)^2}} e^{-r^2/w^2(z)} e^{ik_n r^2/2R(z)} e^{i \arctan\left(\frac{2z}{b}\right)}, \quad (2.8)$$

where a is the amplitude of the electric field envelope, $w(z)$ the spot size and b is the confocal parameter. The spot size is defined for a given longitudinal position as the transverse distance from the propagation axis to where the electric field has decreased by a factor of $1/e$. The spot size at the focus is called the beam waist. The confocal parameter, given by $b = w_0^2 k$, is the distance for which the beam is considered to be collimated.

The actual output of a laser depends on many things; such as the design of the resonator, gain curves of the gain medium, transmission profiles of the windows etc.. However, a paraxial resonator will operate in either Gaussian or spherical mode pending on the stability of the resonator⁸. A stable resonator operates in Gaussian mode. Placing an aperture inside an otherwise stable resonator will perturb the

⁷Where the longitudinal variation of the beam happens at distances much longer than the wavelength.

⁸A stable resonator is defined as resonator, where any injected paraxial ray with respect to the optical axis of the resonator will remain inside the resonator for many in principle infinite number of round trips, while an unstable resonator will increase the transverse offset during each round trip, so that the ray eventually will leave the system.



(a) Beam width and radius of curvature for a Gaussian beam.

(b) Phase variation of a Gaussian beam over the focus.

Figure 2.2: Gaussian beam.

system slightly and allow for a coupling between modes. Since the higher order Hermite-Gaussian modes are spatially wider, they will have higher losses, thus the higher order modes will gradually die out leaving only the lowest order modes[18]. Equation (2.8) is therefore a good approximation of the actual output of a laser system⁹.

Figure 2.2 shows the longitudinal variation of (a) the beam width and wavefront radius of curvature (b) the phase of the fundamental Gaussian mode. It is seen that the on-axis phase of the Gaussian beam changes by $\frac{\pi}{2}$ over the course of the collimation length, while the off-axis effect is less, due to the spherical wave like nature of the Gaussian beams. The on-axis change is called the Gouy phaseshift, and it explains the fact that the beam changes from being spherically converging to spherically diverging as it passes through the focus. The Gouy effect is caused by the transverse confinement of the photons constituting the beam, which leads to a spread in the transverse momentum distribution[19]. The total far field shift is π .

When focusing a collimated beam, which has an approximately flat wavefront, the focal plane is located at a distance from the lens, which is the same as the focal length of the lens. The beam waist w_{02} at the new focus is given by [20]:

$$w_{02} = \frac{f\lambda}{\pi w_{01}}, \quad (2.9)$$

where w_{01} is the beam width at the position of the lens. It is evident from equation (2.9) that shorter wavelengths are focused tighter than longer ones. In particular, a second harmonic generated beam is focused more tightly than the fundamental generating beam, if they have the same size.

Returning to the paraxial wave equation with a source term (2.7), from this equation the field generated through harmonic generation can be determined by taking the source to be the q^{th} mixture of a fundamental field with frequency ω . According to equations (2.1), (2.2) and (2.7) the source term is given as:

$$S_q = \mu_0 \epsilon_0 \chi^{(q)} A_1^q \frac{\partial^2}{\partial t^2} (e^{-i\omega_q t}) e^{i\omega_q t} = \frac{\omega_q^2}{c^2} \chi^{(q)} A_1^q, \quad (2.10)$$

⁹This also explains why lasers usually have a long warm-up time before they operate in single mode.

where $\omega_q = q\omega$ is the frequency of the generated beam and A_1 is the electric field envelope of the fundamental beam.

In principle, similar coupled equations exist for all possible frequency conversions. However, these equations decouple and the harmonic generation for the q^{th} order can be solved separately, under the assumptions that the pump field is undepleted, and the generated fields are weak, such that coupling between the generated frequencies are negligible.

Assuming that the fundamental beam is in the TEM_{00} mode and the harmonic field is initially nonexistent, leads to the situation that the generated beam is also in the TEM_{00} mode with a beam waist which is \sqrt{q} smaller¹⁰.

Insertion of the source term and the TEM_{00} profiles into the paraxial wave equation with these approximations leads to a regular first order differential equation for the electric field envelope amplitude a_q of the q^{th} order field, which can be solved by direct integration yielding[16]:

$$a_q(z) = \frac{iq\omega}{2n_q c} a_1^q \int_{z_0}^z \frac{\chi^{(q)} e^{i\Delta k z'}}{(1 + 2iz'/b)^{q-1}} dz', \quad (2.11)$$

where n_q is the refractive index for the frequency $q\omega$ and z_0 the start of the nonlinear medium. We have allowed for a spatial variation of $\chi^{(q)}$ to account for a possible pressure variation along the nonlinear medium. For a nonlinear medium with constant pressure one usually defines the phase integral J as:

$$J(z) = \int_{z_0}^z \frac{e^{i\Delta k z'}}{(1 + 2iz'/b)^{q-1}} dz', \quad (2.12)$$

with a corresponding generated electric field envelope given by:

$$a_q(z) = \frac{iq\omega}{2n_q c} a_1^q J(z). \quad (2.13)$$

2.3 Quantum mechanical description of the electric susceptibility

The polarization of a medium was earlier defined as the total dipole moment per unit volume. The atomic polarizability is defined as the microscopic expectation of the atomic dipole moment. Using these two definition one can express the polarization in terms of the expectation of dipoles $\langle \boldsymbol{\mu} \rangle$ in the material as:

$$P = N \langle \boldsymbol{\mu} \rangle = N \langle \Psi | \boldsymbol{\mu} | \Psi \rangle, \quad (2.14)$$

where N denotes the number density of atoms and Ψ is the atomic wavefunction which solves the time-dependent Schrödinger equation. This expectation can be calculated using perturbation theory by first writing the wavefunction as a power series of the potential given by interaction of a dipole with an electric field:

$$\Psi = \sum_{i=0}^M \Phi^{(i)}, \quad (2.15)$$

¹⁰As of [21] for the degenerate process of $\omega_1 + \omega_2 + \omega_3 \rightarrow \omega_4$ generalized to q^{th} order.

where (i) denotes the order of the power series and hence the order of the interaction potential, that is needed for the given part of the wavefunction to be applicable. Using this expansion equation (2.14) can be rewritten as:

$$N \langle \Psi | \boldsymbol{\mu} | \Psi \rangle = N \sum_{i,j=0}^M \langle \Phi^{(i)} | \boldsymbol{\mu} | \Phi^{(j)} \rangle, \quad (2.16)$$

this sum can be grouped into terms corresponding to the total interaction order required as:

$$P = N \langle \boldsymbol{\mu} \rangle = N \langle \Phi^{(0)} | \boldsymbol{\mu} | \Phi^{(0)} \rangle + N \sum_{k=1}^M \langle \boldsymbol{\mu}^{(k)} \rangle, \quad (2.17)$$

where k corresponds to the sum of i and j in (2.16), hence each term of $\langle \boldsymbol{\mu}^{(k)} \rangle$ contains $k + 1$ of the terms given in (2.16). The terms where $M < k < 2M$ have been omitted since we are considering perturbations to M^{th} order. The term $N \langle \Phi^{(0)} | \boldsymbol{\mu} | \Phi^{(0)} \rangle$ accounts for a possible polarization in the medium without the presence of the field, and is therefore not associated with the perturbation. We now compare this representation of the polarization with the expansion given in (2.2). It is readily seen that each dipole moment term $\langle \boldsymbol{\mu}^{(k)} \rangle$ is associated with a term of the susceptibility expansion of the same order $\chi^{(k)}$. The actual calculation of the dipole moments and hence susceptibilities is a long task, which requires a more detailed description of time-dependent perturbation theory and is therefore excluded here¹¹, instead the result for the linear susceptibility is merely given[16]:

$$\chi_{ij}^{(1)}(\omega_p) = \frac{N}{\epsilon_0 \hbar} \sum_m \left(\frac{\mu_{gm}^i \mu_{mg}^j}{\omega_{mg} - \omega_p} + \frac{\mu_{gm}^j \mu_{mg}^i}{\omega_{mg}^* + \omega_p} \right), \quad (2.18)$$

where m is the different energy eigenstates (with energies $E_m = \hbar\omega_m$), g is the initial state, $\omega_{mg} \equiv \omega_m - \omega_g$, ω_p is the frequency of the applied field and $\mu_{gm} \equiv \langle g | \boldsymbol{\mu} | m \rangle$, and finally i, j represents the spatial coordinates.

It is clearly seen that calculating the linear susceptibility is a complicated task in itself, but going to the higher order susceptibilities just adds more complexity. Each higher order not only involves another dipole transition between intermediate states, which leads to another sum over the different energy eigenstates, but also increases the number of applied fields by one which amounts to an increase in terms to the number of permutations between the applied fields. As an example the third order susceptibility contains 24 terms; 4 dipole transitions multiplied with the number of permutations for the 3 fields (which is 6). Nevertheless some theoretical calculations of the third order susceptibility have been performed. In figure 2.3 the

¹¹In order to calculate the dipole moments, one first has to calculate the power series for the wavefunction in equation (2.15). Since the requirement of perturbation theory is that the system has been solved in the perturbation free case, eigenfunctions that span a complete basis set exist and are known. So calculating the power series boils down to expanding the $\Phi^{(i)}$ functions unto this set and then calculating the expansion coefficients. It can be shown that the different orders of a given expansion coefficient of a function onto a particular state are linked through the Dyson Series of the perturbation (See [22] chapter 5.6 for details). So one can calculate the expansion of $\Phi^{(0)}$ onto the basis set and then use the Dyson Series to recursively determine the coefficient of the rest of the power series. Deriving the susceptibilities from thereon is a matter of matching the terms.

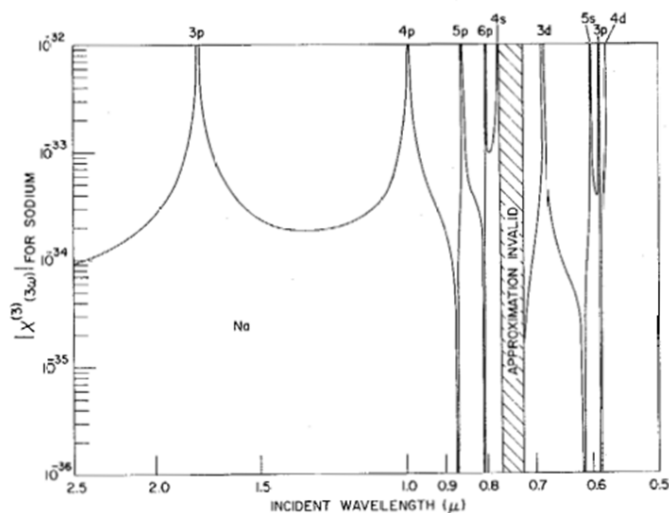


Figure 2.3: Theoretical calculations of $\chi^{(3)}(3\omega)$ for degenerate and polarized fields in sodium vapor. The figure was burrowed from [23].

result of a calculation of the third susceptibility for the case of three degenerate and polarized fields in sodium vapor is shown[23]. The calculation is based on the dipole transition rule that $\Delta l = \pm 1$ under the assumption that the only initially populated level is the ground level, where $l = s$. Also the authors have not included the sum over states where the principal quantum number changes by more than 3 ($\Delta n \leq 3$), which defines the part marked as approximation invalid. These assumptions significantly simplify the calculations. Looking on the figure one notices that the third order susceptibility at a given frequency is usually dominated by the closest resonance peak ω_0 , this trend can be used to give an approximative guess for the third order susceptibility for a frequency ω_a , if one knows the third order susceptibility at another frequency ω_b , which is close to ω_a as¹²:

$$\chi^{(3)}(-\omega_{3a}; \omega_a, \omega_a, \omega_a) \approx \frac{\omega_0 - \omega_{3b}}{\omega_0 - \omega_{3a}} \chi^{(3)}(-\omega_{3b}; \omega_b, \omega_b, \omega_b). \quad (2.19)$$

2.3.1 Nonlinear optics in isotropic materials

In a medium that is isotropic and therefore possesses inversion symmetry, such as for example gases and liquids the even-order nonlinear susceptibilities disappear. For the case of an atomic gas this can be understood in terms of the formulation presented in the previous section. From equation (2.18) and the following discussion it is apparent that the even-order susceptibilities involve an uneven number of dipole transitions. However, according to Laporte's rule for N -electron atoms the parity of the system changes during each dipole transition[25], such that the even-order susceptibilities possess uneven parity, hence the initial and final state cannot be the same under the dipole approximation. The even-order susceptibilities are therefore dipole forbidden and strongly suppressed. One effect of this is that generally only

¹²As of [24] although slightly modified.

Also the notation $\chi^{(3)}(\omega_1 + \omega_2 + \omega_3 \rightarrow \omega_4) \equiv \chi^{(3)}(-\omega_4; \omega_1, \omega_2, \omega_3)$ has been introduced.

uneven ordered harmonics can be generated in a gas through direct processes. Birefringent crystals are per definition not isotropic, hence the above discussion is not a problem that prevents SHG in a birefringent crystal.

The difference between the gas and a birefringent crystal is schematically shown in contour plots on figure 2.4 for an electron in a spherical and a triangular potential, respectively. In (a) and (b) no electric fields are applied, and in average the electron is expected to be at the bottom of either potential, indicated by blue dots. In (c) and (d) time-dependent electric fields polarized in the x direction are applied. In (c) the spherical symmetry of the potential causes the electrons expectation (now marked by a blue line) to oscillate along the x direction according to the applied field, while the expectation along the y direction remains unchanged. In (d) the same thing happens in the x direction, while the expectation in the y direction also changes, because once the electron is moved from the equilibrium position at the center of the potential by the electric field, then the potential is lower in the negative y direction, and hence the electron is accelerated in that direction. This causes a shift in the mean expectation in the y direction indicated by the x' axis. The electron oscillates with twice the frequency of the electric field around this new center position, since the electron returns to the bottom of the potential twice per electric field cycle.

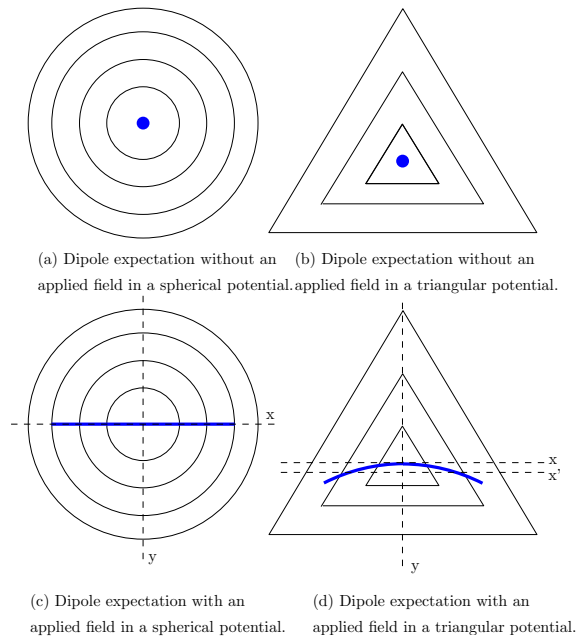


Figure 2.4: Contour plots of the expectation of an electron in a spherical and a triangular potential without an applied field (a),(b) and with an applied field (c), (d).

PHASE MATCHING AND NONLINEAR INDUCED REFRACTIVE INDEX SHIFTS

As indicated by the previously described nonlinear interactions phase matching plays an essential role in every nonlinear interaction. Often the best phase-matched interaction completely dominates the other interactions, it is therefore essential to know how to calculate and manipulate the phase-matching conditions. The following chapter provides a short overview of the processes which can contribute to changes in the refractive index, and thereby the phase of an electric field.

3.1 Sellmeier equations

The Sellmeier formulas are a set of purely empirical equations, which are used to describe the refractive index of a material as a function of wavelength of a light wave passing through it. The equations are based on a least mean square (LMS) fit of experimental data and are usually represented in the following form:

$$n^2(\lambda) = 1 + \sum_i \frac{B_i \lambda^2}{\lambda^2 - \lambda_i^2}, \quad (3.1)$$

where the λ_i can be interpreted as the various resonance lines of the material with B_i as the oscillator strength of these lines[26]. The LMS fits are usually only based on three to five terms. For some materials the equations differ slightly from the general form, but are nonetheless considered to be Sellmeier equations. The equations usually work best far from the absorption lines, since the refractive index is assumed real. Hence a Sellmeier equation is usually defined for a given wavelength range. In figure 3.1 the refractive indices of various inert gases are plotted[27].

3.2 Group velocity and GVD

In addition to giving a wavelength dependent relationship of the refractive indices, the Sellmeier equations also have proven to be an excellent source for approximate determination of the group velocity and group velocity dispersion (GVD) of an electromagnetic pulse passing through the medium. GVD is the effect that the

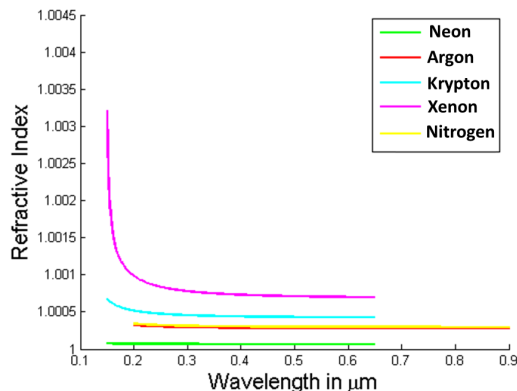


Figure 3.1: Tabulated Sellmeier equations for various inert gases.

various spectral components of a pulse in a dispersive medium experience different refractive indices, and therefore move at different speeds.

A pulse for which the time-bandwidth product is limited by the uncertainty principle is called Fourier transform limited (or simply transform limited), while a pulse which is longer than the transform limited duration is said to be chirped. One usually distinguishes between positive and negative chirp, where a positive chirp means that the instantaneous frequency¹ increases with time, while a negative chirp means a decrease with time.

Due to the time-bandwidth product GVD becomes increasingly relevant for ultrashort pulses. Also pulses with shorter center wavelengths are usually more subjective to GVD due to the normal dispersion described in the previous section. Dispersion can be expressed in mathematical terms by assuming that the dispersion of the spectral components are small with respect to the center frequency ω_0 . In this case the propagation constant k for a given frequency ω can be expressed in the form of a Taylor expansion:

$$k(\omega) = k(\omega_0) + \left. \frac{\partial k}{\partial \omega} \right|_{\omega_0} (\omega - \omega_0) + \frac{1}{2} \left. \frac{\partial^2 k}{\partial \omega^2} \right|_{\omega_0} (\omega - \omega_0)^2 + \dots \quad (3.2)$$

The link to the Sellmeier equations comes into play by using the relation $k(\omega) = \frac{\omega}{c} n(\omega)$. The phase velocity of a given frequency is therefore $v_\phi(\omega) = \frac{\omega}{k(\omega)}$, the group velocity v_g which describes the velocity of the pulse envelope is related to the second term of the expansion as $v_g^{-1} = \left. \frac{\partial k}{\partial \omega} \right|_{\omega_0}$, while the third term describes group velocity dispersion with $k'' = \left. \frac{\partial^2 k}{\partial \omega^2} \right|_{\omega_0}$.

A medium for which $k'' > 0$ in the optical regime is called normally dispersive and is caused by the fact that strong resonances usually are localized in the ultraviolet part of the spectrum². On the other hand if $k'' < 0$ for optical wavelengths the medium is called anomalous dispersive³.

¹Defined as the time derivative of the phase.

²For example for molecules the resonances correspond to excitation of vibrational and rotational modes, as well as electronically transitions. The former two normally lie in the infrared part, while the latter lie in the ultraviolet end[28].

³The terms normal and anomalous dispersive stems from the fact that most materials follow this trend in the optical part of the electromagnetic spectrum and historically the refractive indices was first investigated in this part of the spectrum. A medium can be normal dispersive in one region and anomalous in another.

In general GVD leads to a symmetric broadening of an unchirped pulse, since either the red or the blue part of the pulse will have faster phase velocity depending on whether the medium exhibits normal or anomalous dispersion, respectively. A chirped pulse can be recompressed by propagation in a dispersive medium with the opposite sign of GVD. For pulse duration shorter than 30 fs even higher order terms of the Taylor Series are usually needed[29], the lowest of which breaks the symmetry of a Gaussian pulse[30].

3.3 Refractive index corrections

The Sellmeier equations are usually fitted to some particular conditions, such as for a given pressure and temperature. Normally, one would like to know the refractive index under different conditions. This can be done by looking at the very nature of the refractive index. The index was introduced in the beginning of chapter 2 as $n^2 = 1 + \chi$. For a weak electric field the susceptibility is replaced by the first order susceptibility, which is proportional to the number density N (section 2.3) so $n^2 - 1 \propto N$. The number density of an ideal gas is given by $N = \frac{p}{k_b T}$, where p is the pressure of the gas, T the temperature and k_b is the Boltzmann constant. If we assume that $n(p_0, T_0) \equiv n_0$ is known, the refractive index at other temperatures and pressures can be determined from the following relation:

$$\frac{n_0^2 - 1}{n^2 - 1} = \frac{p_0 T}{p T_0}, \quad (3.3)$$

where n denotes the refractive index at pressure p and temperature T . At high pressures or dense materials this equation is slightly modified by the local electric field caused by polarization of nearby atoms[31]. This is known as the Clausius Mossotti relation. The correction is minor for gases and thus avoided here but nonetheless used in the simulations in chapter 4.

3.3.1 Nonlinear refractive index

For obvious reasons the description of the refractive index given in this chapter is still not complete, since the nonlinear interactions are yet to be accounted for. In the following we assume that the medium is isotropic, such that the lowest nonlinear contribution to the susceptibility is the third order contribution. Consider the process of $\omega + \omega - \omega \rightarrow \omega$, this is a third order nonlinear process, which generates a polarization field at the fundamental frequency. This effect is described by the frequency decomposed equivalent of the third order term given in equation (2.2). For an electromagnetic beam propagating along the z -axis, the polarization of the electric field lies in the x, y plane, so the summations are hence reduced to summations over the x, y coordinates. In frequency space the third order polarization which leads to this effect is therefore given by:

$$\begin{aligned} \frac{1}{\epsilon_0} P_i^{(3)}(\omega) &= \sum_{j,k,l=x,y} \chi_{ijkl}^{(3)} E_j(\omega) E_k(\omega) E_l(-\omega) = \sum_{k,l=x,y} \chi_{iikl}^{(3)} E_i(\omega) E_k(\omega) E_l^*(\omega) \\ &+ \sum_{j,l=x,y} \chi_{ijil}^{(3)} E_j(\omega) E_i(\omega) E_l^*(\omega) + \sum_{j,k=x,y} \chi_{ijkj}^{(3)} E_j(\omega) E_k(\omega) E_i^*(\omega), \quad (3.4) \end{aligned}$$

where $E(-\omega) = E^*(\omega)$ have been used. If the light is linearly polarized along the x -axis then $i = j = l = k = x$, and only the x -components of the summations remain. The generated polarization therefore reduces to $P_x^{(3)}(\omega) = 3\epsilon_0\chi^{(3)}|E_x(\omega)|^2E_x(\omega)$, where $\chi^{(3)} \equiv \chi_{xxxx}^{(3)}$.

Including the linear susceptibility, the frequency effectively feels a linear susceptibility given by: $\chi_{\text{eff}}^{(1)} = \chi^{(1)} + 3\chi^{(3)}|E_x(\omega)|^2$. The refractive index of a material can in general be described by a linear relation with intensity as[16]:

$$n = n_0 + n_2I = n_0 + \frac{1}{2}n_2n_0\epsilon_0c|E(\omega)|^2, \quad (3.5)$$

where n_0 is the normal refractive index, while n_2 is the proportionality constant of the nonlinearity. Using the relation $n^2 = 1 + \chi_{\text{eff}}^{(1)}$, n_2 can then be determined as:

$$n^2 = (n_0 + n_2I)^2 = 1 + \chi^{(1)} + 3\chi^{(3)}|E(\omega)|^2 \Rightarrow n_2 \approx \frac{3\chi^{(3)}}{n_0^2\epsilon_0c}, \quad (3.6)$$

where terms of second order in $|E(\omega)|^2$ have been omitted. In the case of two beams with frequencies ω_1, ω_2 with the DFG of $\omega_1 + \omega_2 - \omega_2 \rightarrow \omega_1$ the nonlinearity is twice as strong on the passive as compared to the interacting beam, this is due to the degeneracy of the active beam[16], in this case n_2 becomes:

$$n_2^{\text{cross}}(\omega_1) = \frac{6\chi^{(3)}}{n_0^2\epsilon_0c}, \quad (3.7)$$

where n_2^{cross} is called the cross coupling nonlinear refractive index.

An essential consequence of the nonlinear refractive index for ultrafast optics is the effect called self-phase modulation (SPM). Since the light waves in ultrafast optics are pulses the nonlinear refractive index and the refractive index become time-dependent. This time-dependence of the refractive index leads to a chirp of the pulse, as the instantaneous frequency becomes time-dependent. For an optical pulse with an electric field given by $E(t, x) = E_0e^{i(\omega_0t - kx)}$ the instantaneous frequency is given by:

$$\omega(t) = \frac{\partial}{\partial t}\phi(t) = \frac{\partial}{\partial t}\left(\omega_0t - \frac{\omega_0}{c}n(t)x\right) = \omega_0 - \frac{\omega_0}{c}n_2x\frac{\partial I(t)}{\partial t}, \quad (3.8)$$

where $I(t)$ is intensity of the electric field envelope. Equation (3.5) has been used in deriving the last step of (3.8). It is clear that the different temporal parts of the pulse will experience different frequency shifts. Neglecting reshaping of the pulse due to SPM, then SPM leads to a symmetric broadening of a compressed pulse. Since the nonlinear refractive index in general is positive, the leading parts of the pulse, for which the intensity slope is rising, are red-shifted, while the trailing parts of the pulse are blue-shifted.

3.3.2 Plasma contribution to the refractive index

If the applied field becomes too intense the atoms and molecules in the dielectric material start to be ionized, resulting in free charges in the form of ions and free electrons. This causes the electric response of the medium to change into the behavior of a conducting material. Since the electrons are much lighter than the ions they

contribute the most to the conductivity, which leads to a decrease in the electric permittivity, and thereby a decrease in the refractive index.

Unfortunately, this decrease is greater for lower frequencies than for higher. So in the case of normal dispersion, this effect actually degrades the phase-matching conditions, and should therefore be avoided.

For low concentration of free electrons the plasma induced dispersion results in a refractive index change of[28]:

$$\Delta n_{\text{plas}}(\omega) = -N_e \frac{e^2}{2m_e \epsilon_0 n_0 \omega^2}, \quad (3.9)$$

where N_e is the free electron density, m_e the electron mass and n_0 is the refractive index before the change.

A temporal treatment of the ionization process shows that the generation of free electron leads to a refractive index which decreases with time, which leads to a blue-shift of the pulse[32]. Since the pulse itself is the driving force of the ionization process, the leading parts of the pulse are less affected by the free electrons, and the front edge is therefore less blue-shifted. If the pulse is intense enough the generation of free electrons is saturated by total ionization of the medium, after which the remaining parts of the pulse are identically blue-shifted.

Figure 3.2 schematically shows the difference between the shift of the instantaneous frequencies caused by self-phase modulation and the generation of free electrons.

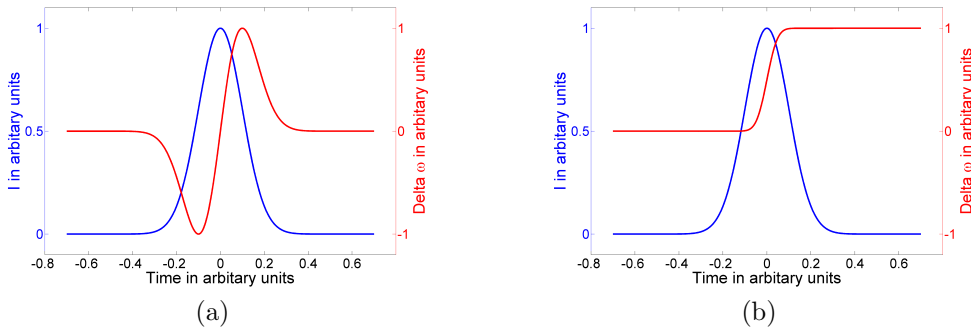


Figure 3.2: Schematic illustrations of how the different temporal parts of an optical pulse is effected by: (a) Self-phase modulation. (b) Free electron dispersion.

3.3.3 Modal dispersion in a waveguide

One way of obtaining phase-matching conditions is to make use of waveguides. In waveguides light propagates differently compared to free space due to the geometrical aspect of a waveguide, which changes the boundary conditions for the light wave. The modified boundary conditions cause the modal basis set of the waveguide to be different, which leads to altered dispersion relations. Assuming that the field is propagating in the forward z -direction, the electric field inside the waveguide can be written as:

$$E(x, y, z) = \sum_{n,p} A_{n,p} B_{n,p}(x, y) \exp(-i\beta_{n,p}(z - z_0)), \quad (3.10)$$

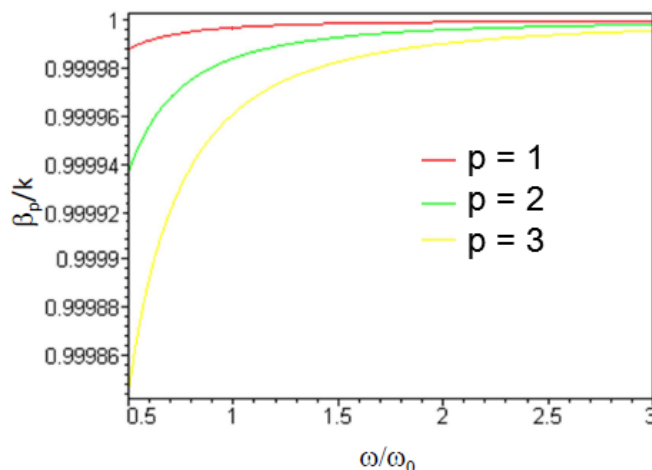


Figure 3.3: Dispersion in a hollow capillary.

where $A_{n,p}$ is the amplitude of the various modes, $B_{n,p}$ is the transverse distribution, z_0 is the start of the waveguide, and $\beta_{n,p}$ is the so-called propagation constant. The amplitude of the various modes depends on the overlap integral between the input field E_{in} and the mode at the boundary between free space, and the start of the waveguide, so:

$$A_{n,p} = \langle B_{n,p}(x, y) | E_{in}(x, y, z_0) \rangle. \quad (3.11)$$

In order to use the weakly dispersive nature of gas, and limit the amount of absorption, a hollow dielectric cylinder backfilled with gas, was used as a waveguide in this thesis. For a so-called hollow capillary the propagation constant is given by [33, 34]:

$$\beta_{n,p} = k_0 \sqrt{1 - \left(\frac{u_{n,p}}{ak_0} \right)^2}, \quad (3.12)$$

where k_0 is the free space wavenumber, a is the radius of the capillary, and $u_{n,p}$ is the p 'th root of the $n - 1$ order Bessel function $J_{n-1}(u)$. The propagation constant is in general a complex number, which for $ak_0 < u_{n,p}$ has an imaginary part, which corresponds to an attenuation of the mode. For transverse magnetic and electric hybrid modes⁴ the attenuation constant $\alpha_{n,p}$ is given as:

$$\alpha_{n,p} = - \left(\frac{u_{n,p}}{k_0 a} \right)^2 \frac{1}{2a} \frac{1 + n_c^2}{\sqrt{n_c^2 - 1}}, \quad (3.13)$$

where n_c is the refractive index of the cladding. As apparent from equation (3.12) the higher order modes (for which $u_{n,p}$ is large) have a shorter propagation constant, which allows for a way of circumventing the normal dispersion, and obtain phase-matching between the fundamental frequency light, and light with the third harmonic frequency. The phase-matching can be obtained by coupling the fundamental frequency light into the fundamental waveguide mode, while the third harmonic light would be generated at certain higher order modes. The propagation constant is plotted for the first few modes of $n = 1$ in figure 3.3. The red curve is the lowest order mode, while the green and yellow curves respectively are the second and third lowest order modes.

⁴Modes with $n \neq 0$.

NUMERICAL SIMULATIONS

In order to help designing the experimental setup, a numerical model was required. The model had to be able to predict how third harmonic generation of an ultrashort pulse focused inside a gas cell depends on the following parameters; pulse energy, gas pressure, position of the laser focus, the confocal parameter, and the cell length.

A number of different models for nonlinear pulse propagation can be found in the literature[32]. The majority of these schemes are based on the so-called split-step models, in which the nonlinear propagation is divided into linear and nonlinear parts, which are propagated separately. The split-step models are normally divided into two types; time-propagation[35] and frequency-propagation[36].

In spectral propagation codes the linear step can be exactly performed in frequency space after 3-dimensional Fourier transform of the field, while the nonlinear step is handled in normal space. In time-propagation schemes both the linear and nonlinear steps are performed in normal space, this method generally requires smaller propagation steps, and dispersion is at the same time not treated precisely. Both types of nonlinear propagation codes are considerably time-consuming both in derivation and in implementation, and were therefore not well suited for our purposes.

Instead a simple phase-matching code was derived, which allowed for preliminary simulations of the expected effects of the various experimentally changeable parameters.

The simulation was carried out in Matlab for ultrashort laser pulses with a center wavelength of 800 nm. The pulses were focused into a gas cell filled with a constant pressure of argon, placed in the middle of a one meter long vacuum tube, with a fixed pressure ratio between the tube p_t and the cell p_c . At the boundary between the cell and the tube, the gas pressure was assumed to follow the Gaussian error function, which is a steady state solution to the diffusion equation.

The electric field amplitude of the generated third harmonic light by a focused Gaussian pump pulse at the end of the vacuum tube is given by equation (2.11) with $q = 3$, $z_0 = 0$ m and $z = L = 1$ m, i.e.:

$$a_3 \propto \int_0^L \frac{\chi^{(3)} e^{i\Delta k(z'-z_f)}}{\left(1 + i2\frac{z'-z_f}{b}\right)^2} dz', \quad (4.1)$$

where z_f denotes the focal position of the pump.

The third order susceptibility was calculated from tabulated values of the third order hyperpolarizability¹ $\gamma^{(3)}$ in the presence of the fourth order local field correction L_4 as[24]:

$$\chi^{(3)} = \frac{p}{\epsilon_0 k_b T} \gamma^{(3)} L_4. \quad (4.2)$$

The wave vector mismatch for THG is given by:

$$\Delta k = 3k(\omega) - k(3\omega) = 3 \frac{2\pi}{\lambda} (n(\omega) - n(3\omega)), \quad (4.3)$$

the refractive indices were calculated using equations (3.5), (3.6), (3.9) and (4.2) as well as the correction due to localized fields as:

$$n_{tot}(\omega') = n_p L_1 + \frac{p}{\epsilon_0 k_b T} \frac{3\gamma^{(3)}}{n_p^2 \epsilon_0 c} I L_4 - N_e \frac{e^2}{2m_e \epsilon_0 n_p (\omega')^2}, \quad (4.4)$$

where L_1 is the first order local field correction, n_p is the refractive index at a given pressure, temperature and frequency given by the Sellmeier equation for argon in combination with equation (3.3). The tabulated values of $\gamma^{(3)}$ were taken from [24], in which it was measured for $\lambda = 1055$ nm. The third order susceptibility was therefore brought to 266 nm and 800 nm by the use of equation (2.19).

4.1 Estimation of the plasma density

A simulation² of the number density of free electrons in a 30 mm gas cell filled with different pressures of argon as a function of propagation distance is shown on part (a) of figure 4.1, while part (b) of the figure shows the corresponding spatial dependent fluence³. The cell was exposed to a short pulse ($\lambda = 800$ nm, $E = 450$ μ J, $\tau = 30$ fs) focused down to a vacuum spot size⁴ of 20 μ m. This would correspond to an intensity, a fluence and a confocal parameter of roughly $2 \cdot 10^{15}$ W/cm², 70 J/cm², and 3 mm, if focused in vacuum.

The photoionization rate in this simulation was based on the generalized Keldysh PPT theory, while the instantaneous fluence was calculated by a Fourier split-step frequency-propagation scheme[37].

Comparing the two figures it is seen that once the free electron density exceeds $5 \cdot 10^{17}$ cm⁻³, the fluence reaches a saturation level, even before the pulse reaches the geometrical focus. This is due to plasma-defocusing. Consequently plasma defocusing limits the maximum intensity of a focused ultrashort laser pulse in a gas. For 1 bar of argon the maximal intensity becomes $\sim 1.5 \cdot 10^{14}$ W/cm², while the intensity can grow higher at lower pressure. One also notices that the total density of free electrons near the focus is roughly the same in all cases. At 1 bar the ionization in this simulation corresponds to a relative ionization of approximately 5%, while the ionization level at 50 mbar was about 70%.

Finally one notices that the fluence of the pulse maintains the saturation level over a considerable distance. This is caused by the formation of a self-guiding

¹The third order hyperpolarizability is defined as the third order polarizability of a single atom.

²Provided by Cord L. Arnold.

³Defined as $F = \int I dt$.

⁴The spot size that would be obtained if not for self-focusing, plasma-defocusing etc..

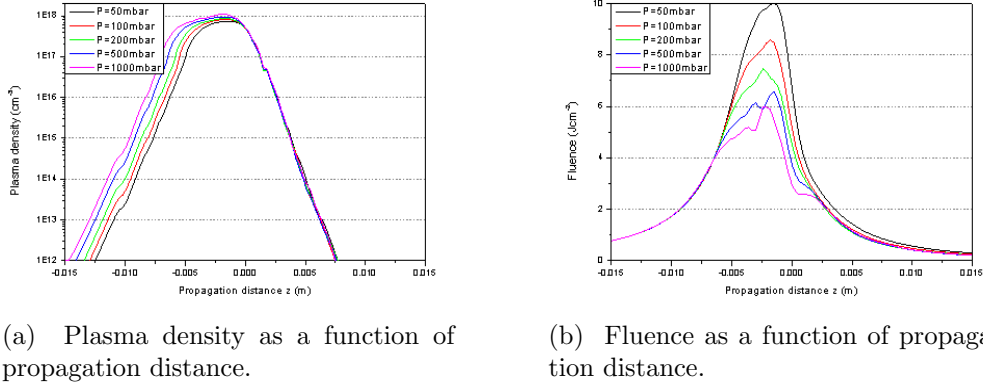


Figure 4.1: Simulation of the plasma density as a function of the propagation distance in 3 cm long gas cell for a 800 nm, 450 μJ , 30 fs pulse focused down to freespace spot size of 20 μm .

filament by the interplay between the nonlinear refractive index, multi-photon absorption and free electron dispersion[32].

The simulations conducted in this report, were not time dependent; so actual calculations of the plasma density, pulse shape etc. was not performed; the surrounding parameters were instead chosen such that the pulse behaves in a simple Gaussian way. From the simulations described above the intensity at the focal point had to be limited to 10^{14} W/cm^2 , so the pulse energy was chosen such that with the tightest focusing (shortest confocal parameter) the intensity would not exceed this level.

Table 4.1: Parameters for numerical simulations.

Pulse energy	170	μJ
Pulse length	30	fs
Central wavelength	800	nm
Temperature	300	K
Pressure ratio	10^{-3}	
$\chi^{(3)}(\omega)$	$7 \cdot 10^{-26}$	Cm^4/V^3
$n_0(\omega)$	1.0003	
$n_0(3\omega) - n_0(\omega)$	$2.1 \cdot 10^{-5}$	
$n_2(\omega)$	$2.5 \cdot 10^{-23}$	m^2/W
$n_2(3\omega)$	$2.8 \cdot 10^{-23}$	m^2/W

The simulations for THG were carried out for cell lengths between 6 and 15 mm with confocal parameters of 1-10 cm. The intensity is thus approximately constant within the gas cell. Consequently, the relative ionization was assumed not to vary along the cell. To account for the pressure difference between the cell and the vacuum chamber and to avoid an increase in the plasma density at the boundary,

the density was set to be:

$$N_e = \frac{p}{50\text{mbar}} 5\% N_a \text{m}^{-3} \quad \text{for } \max(p_c) < 50\text{mbar}, \quad (4.5)$$

$$N_e = \frac{p}{\max(p_c)} 5\% N_a \text{m}^{-3} \quad \text{for } \max(p_c) > 50\text{mbar}, \quad (4.6)$$

where p denotes the pressure at a particular place and N_a is Avogadro's constant. In table 4.1 the rest of the parameters used for all simulations are shown.

4.2 Simulation of THG light

Equation (4.1) was solved numerically using the trapezoidal routine⁵ implemented in Matlab. The code was written such that for a given confocal parameter, cell length L_c , and pressure Matlab solves the integration a number of times for different choices of focal position.

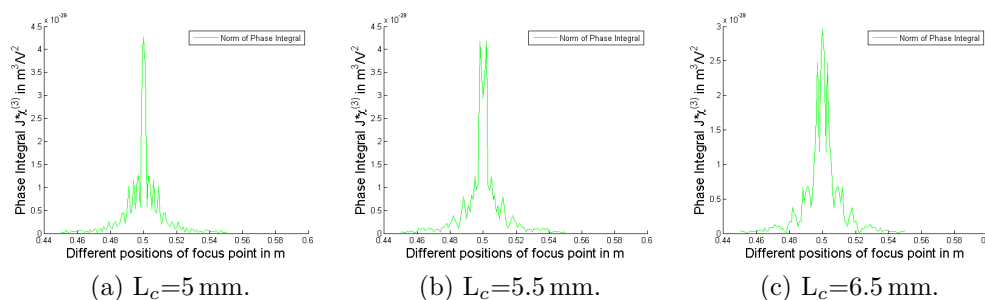


Figure 4.2: Phase integrals at various cell lengths L_c for $p = 1$ bar, $b = 1$ cm.

A series of such calculations are shown in figure 4.2 for short cell lengths. It is seen that the optimum focal position varies with the length of the cell, and in general the position is either at the center of the cell or very close to it. The intensity is therefore maximized across the medium.

Figure 4.3 demonstrates the behavior of the phase integral in a condensed way. Each point in this figure corresponds to a calculation of the type shown in figure 4.2. The green curve shows the efficiency for the focal plane located at the center of the cell, while the red and blue curves respectively show the minimal and maximal efficiencies for the various focal positions. An oscillation of the green curve is clearly visible, and is caused by a wave vector mismatch between the driving field and the generated field. If we for a moment disregard the nonlinear contribution to the refractive index, then the wave vector mismatch inside the cell is constant and given by $7.7 \cdot 10^3 \text{ m}^{-1}$, which corresponds to a coherence length of $8.1 \cdot 10^{-4} \text{ m}$. The generated signal therefore oscillates with frequency of the coherence length, when the cell length and thereby propagation distance is varied.

However, the intensity is not constant across the medium, so when taking into account the nonlinear refractive index, an additional spatially dependent mismatch is added. In figure 4.3 the focusing is rather loose, so the additional mismatch caused

⁵In the trapezoidal routine the integration interval is divided into a number of uniform subintervals. Each subinterval of the integration is then approximated by a trapezoid. The integration is then performed by calculating the area of these trapezoids.

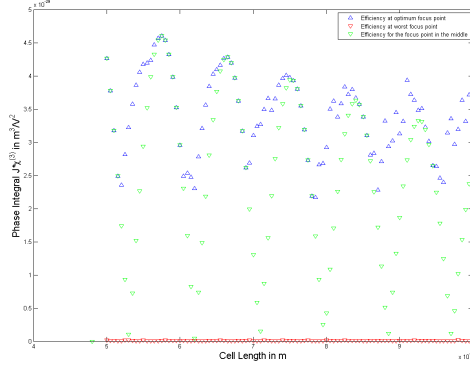
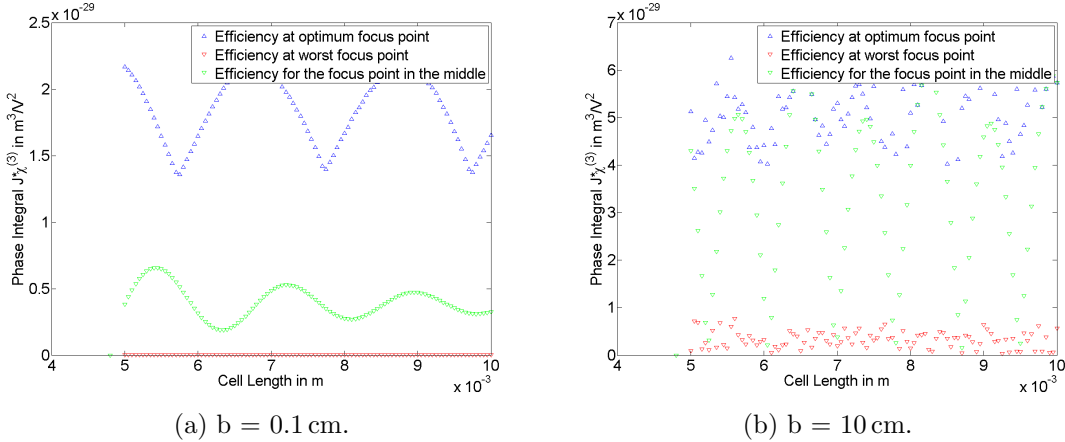


Figure 4.3: Phase integral variation for L_c between 5 and 10 mm, $b = 1$ cm, $p = 1$ atm.

by the nonlinear contribution is $2.6 \cdot 10^2 \text{ m}^{-1}$ at the focus, which is insignificant when compared to the spatially independent mismatch. Hence a change in the oscillation period is not seen. However, the shift in oscillation frequency is clearly visible on part (a) of figure 4.4, where a ten times tighter focusing causes a strongly spatially dependent shift of the wave vector mismatch. At the focal position this shift is $2.6 \cdot 10^3 \text{ m}^{-1}$, which is of the same magnitude as the spatial independent mismatch.



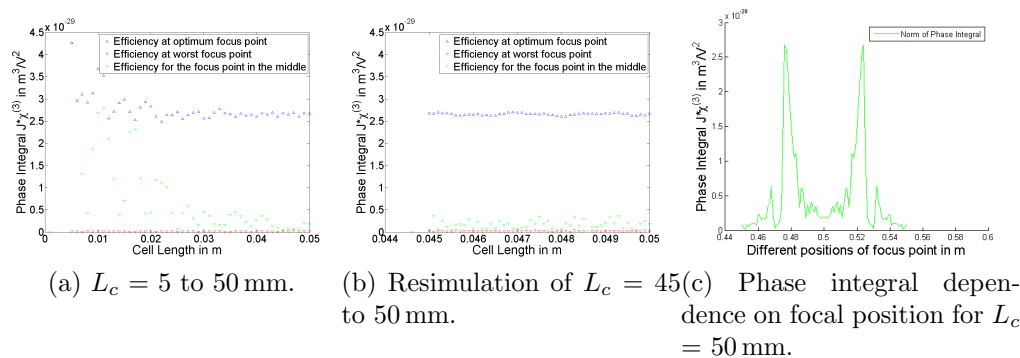
(a) $b = 0.1$ cm.

(b) $b = 10$ cm.

Figure 4.4: Effects of changing the confocal parameter. $p = 1$ bar, $L_c = 5$ to 10 mm.

The opposite case of even looser focusing is shown in part (b) of figure 4.4. The result looks almost identical to figure 4.3, even the magnitude of the phase integral is of the same order, which suggests that loose focusing with a higher power beam might be the way to go.

On part (a) and (b) of figure 4.5 the effects of changing the cell lengths are shown. It is seen that for longer cell lengths the optimum focal position shifts from the center of the cell. The ratio between the confocal parameter and the cell length seem to be the deciding factor for this, when comparing with the similar result shown in part (a) of figure 4.4, which were taken for shorter values L_c and b . In part (c) of figure 4.5 the phase integral for a confocal parameter to cell length ratio of $1/5$ is shown. The optimum focus position has in this case changed from the center of the gas cell into two peaks, one right at the start of the cell and one right at the


 Figure 4.5: Effects of cell length. $p = 1$ bar, $b = 1$ cm.

end. The focal position dependence of the phase integral looks similar for all the other points represented in part (b) of figure 4.5.

The change from the loose focusing behavior can be explained in terms of the Gouy phaseshift. Over the course of the geometrical focus the driving polarization goes through a phaseshift of 3π , since we have three fields, while the generated polarization only experiences a phaseshift of π . Thus a phase slip between the two fields occurs, which causes a destructive interference between light generated at the different parts of the medium[21].

By changing the focal position to either end of the nonlinear medium the symmetry around the geometrical focus is broken, such that the majority of the beam is generated by either a diverging or converging beam, thus the different parts of the generated signal are more in phase.

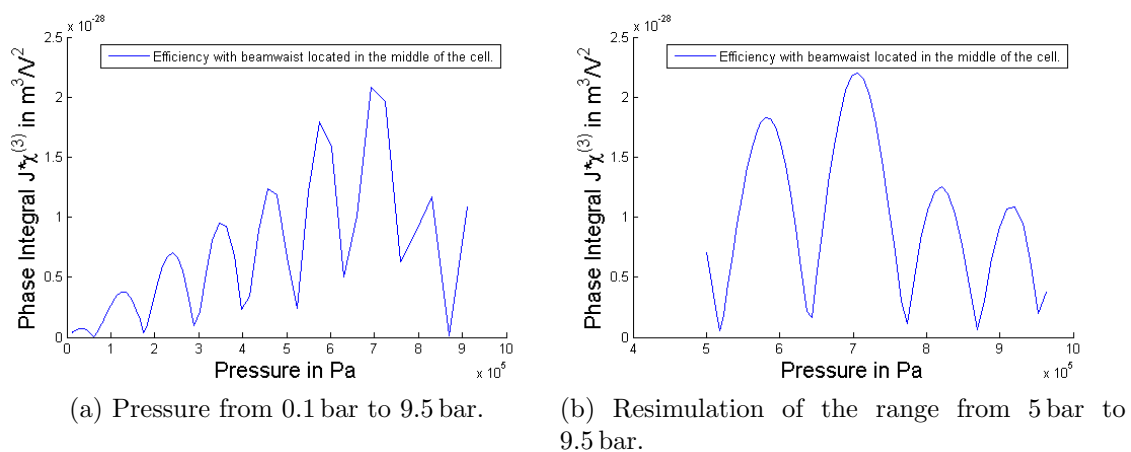

 Figure 4.6: Pressure dependence of the phase integral for 0.1 bar to 9.5 bar, $L_c = 5$ mm, $b = 1$ cm and focal position at the center of the cell.

Figure 4.6 shows how pressure variations effect the phase integral for a given focal position, cell length, and focusing strength. Periodic pressure driven oscillations are clearly apparent, with a period of about 1 bar. A optimum pressure for the THG process seem to be a cell pressure of roughly 7 bar, however one would probably have to account for absorption at such high pressures. Also the setup described in the

next chapter cannot handle such high pressures. Nevertheless tuning the pressure evidently provides a possibility to change the phase mismatch by an integer amount of 2π .

To summarize the conclusions of these simulations, one should aim for high pressure and short cells with loose focusing, and then fine adjust the wave vector mismatch by changing the pressure. If one uses a longer cell, then the geometrical focus of the pump beam should be located at one of the ends of the cell to break the symmetry, preferably at the entrance, where nonlinear effects have not yet distorted the beam.

THE EXPERIMENT

The experimental part of this project was conducted at the Lund High-Power Laser Facility using a 1 kHz, Ti:Sapphire, Chirped Pulse Amplification (CPA) based laser system. The characteristics of the pulses delivered by the system is shown in table 5.1. The system is normally operated at output pulse energies around 3 mJ. The following chapter consists of a general overview of the laser system and vacuum systems used for this project, followed by a description of the various conducted experiments.

5.1 Detailed description of the laser system

The original laser system was delivered in 1998 by B.M. Industries & Thales and has since then been upgraded twice. The first one was in 2006 where the amplifiers were upgraded, while the second one was in 2009 when the overall stabilization were vastly improved in order to obtain a millijoule carrier-envelope phase¹ (CEP) stable CPA laser. Yet another upgrade is currently scheduled for this fall.

¹The offset between the phase of the carrier wave, and the envelope of the pulse.

Table 5.1: Characteristics of the 1kHz laser pulses.

Output from the Oscillator	
Pulse energy	5 nJ
Repetition rate	76 MHz
Laser output post amplification	
Pulse energy	< 6 mJ
Repetition rate	1 kHz
Beam width (1/e)	6.4 mm
Pulse duration	30-35 fs
Center wavelength	800 nm
Spectral FWHM	30-35 nm

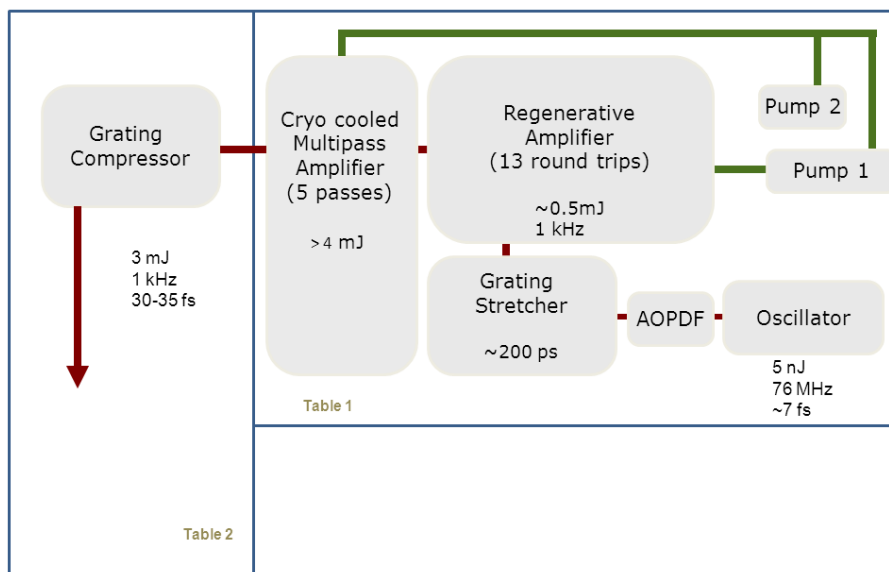


Figure 5.1: Block diagram of the laser system.

Figure 5.1 schematically illustrates the system in its present state[38]. It consists of a CEP stable oscillator, a grating based stretcher followed by two subsequent amplification stages and then finally a grating based compressor.

5.1.1 The oscillator

The active medium of the oscillator is a titanium doped sapphire crystal ($\text{Ti:Al}_2\text{O}_3$), simply called titanium sapphire crystal. The crystal is pumped at 532 nm by a frequency doubled continuous wave (CW) $\text{Nd}_{3+}:\text{YVO}_4$ laser².

The gain profile of a titanium sapphire crystal is centered at 800 nm with a very broad bandwidth ranging from 650 nm to 1100 nm. However, due to gain bandwidth narrowing inside the oscillator along with the spectral bandwidth of the dispersion compensation, the compressed output of the oscillator is about 7 fs long with a bandwidth of about 200 nm. The dispersion compensation is handled through the use of multilayer coated mirrors (also known as chirped mirrors) inside the cavity[39].

A periodically poled lithium niobate (PPLN) crystal is placed outside the oscillator cavity. When the laser is running in CW mode nothing happens inside the PPLN crystal, however whenever the laser is mode-locked, the enhanced intensity causes strong simultaneous self-phase modulation of the fundamental light along with SHG and DFG, this leads to light with overlapping frequencies generated by the different processes. By looking for a beat signal within the overlapping frequencies (see figure 5.2) one can determine whether or not the laser is mode-locked. A dichroic mirror after the PPLN crystal acts as a beam splitter reflecting the red parts of the near-infrared beam while transmitting the blue parts. The reflected parts are the output from the oscillator, while a photodiode measures the CEP

²Neodymium-doped yttrium vanadate.

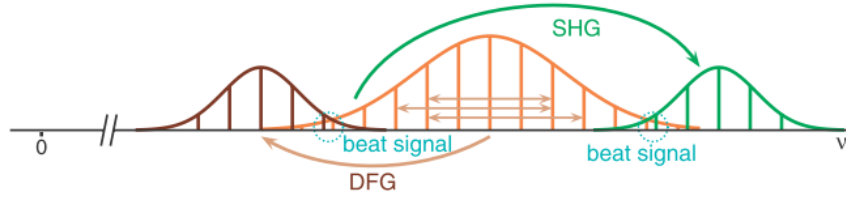


Figure 5.2: Illustration of the principle of CEP detection. SPM leads to a broadening of the frequency comb of the fundamental seed pulse, while DFG leads to an additional redshifted frequency comb and SHG generates a blueshifted frequency comb. When the nonlinear interaction is strong enough parts of the fundamental comb overlaps with parts of the other combs, which causes an interferometric beating by the CEP that can be detected by a photodiode. The figure was borrowed from [41].

from the transmitted parts. If the beating is constant, the oscillator runs in CEP stable mode [40].

In order for the laser to work in pulsed operation, the phases of the different spectral components have to be locked in phase. The general way of obtaining this is by designing the cavity in such a way that CW operation has higher losses than pulsed operation, and thereby causing pulsed mode to be favorable. In our specific case this is obtained by the technique termed Kerr lens mode-locking. In Kerr lens mode-locking one makes use of the optical Kerr effect, which causes the refractive index of the titanium sapphire crystal to be intensity dependent. Due to the Gaussian spatial intensity distribution of a light pulse in a stable oscillator, and the positive nonlinear refractive index of sapphire, the crystal approximately acts a lens with a focal length that is shorter for higher intensities[26]. The oscillator was therefore designed such that a self-focusing beam has lower losses, and the laser prefers the pulsed operation.

The mode-locking process itself starts if several spectral components by accident have the same phase at the crystal and thereby temporally increases the intensity, causing them to lock together in phase due to the favorability of the self-focused beam. Shortly after more and more spectral components swiftly join the pulse, and the short mode-locked pulse is obtained almost instantly after the process has begun.

When turned on the laser starts to heat up the optical components causing thermal fluctuations and thereby modifying the beam path inside the cavity, this continuous change in the optical path prevents mode-locking. The laser therefore usually requires at least one hour of warmup time for the components to settle at a constant temperature before mode-locking can be achieved.

Once this has happened one in principle has to wait for a short temporal quality drop of the cavity in order to disrupt the pulse propagating inside the otherwise now stable CW-mode running laser, before mode-locking happens. A general procedure to speed up the process is by inducing a small perturbation to the cavity and thereby changing the phase of the different spectral components, in our case this is done by gently moving the end mirror of the cavity.

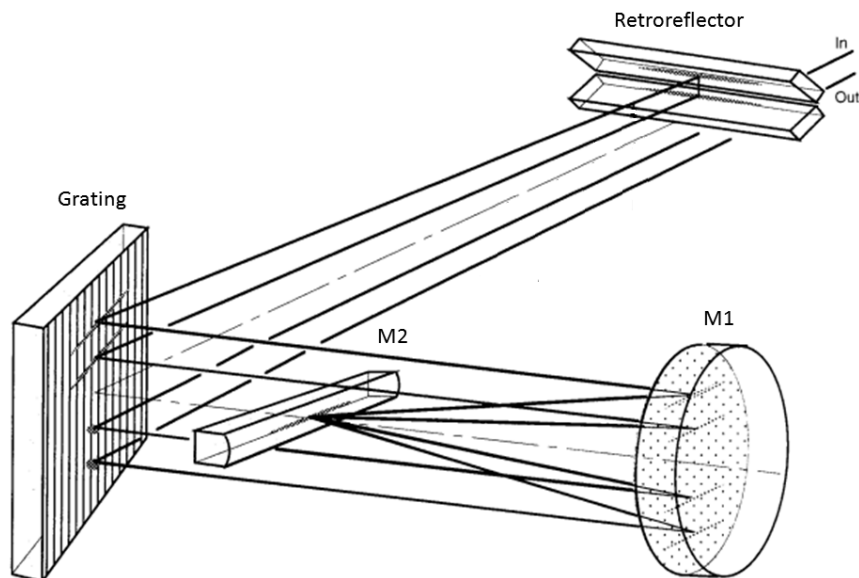


Figure 5.3: Schematic overview of a typical Öffner stretcher[44]. The pulse is sent into a diffracting grating twice per round-pass. The pulse hits the grating immediately after entering the stretcher, while an aberration free inverting one-to-one telescope (telescope with magnification equal to -1) mirrors the first order diffracted pulse onto a different part of the grating, and a retroreflector provides a second pass. From the point of view of the diffracted pulse the beam path corresponds to an antiparallel (see figure 5.4 for definition) grating configuration, which causes a positive GVD and leads to a stretching in time.

5.1.2 The stretcher

After leaving the oscillator, the mode-locked pulse passes through an Acousto Optic Programmable Dispersive Filter (AOPDF, DAZZLER from Fastlite). The AOPDF gives the possibility to select and modify which spectral parts of the seed pulse from the oscillator that will be sent towards the stretcher and the amplifiers, by acting like a bandpass filter with controllable attenuation for the transmitted parts. As one can imagine the AOPDF has several uses; first and foremost it provides the possibility to modify the spectral shape of the seed pulse in order to counteract the effects of gain narrowing inside the amplifiers[42] described below; second it, as the name implies, allows for fine control the phase and thereby dispersion of the different spectral parts of the pulse; third, it can be used to fine tune the central wavelength of the final post compression pulse while maintaining the spectral width simply by modifying the spectral distribution of the seed accordingly[43].

In order to limit the nonlinear processes in the amplification the pulse is after the AOPDF sent towards a stretcher, where the pulse duration is stretched to roughly 200 ps. The stretcher consists of a double-pass triplet Öffner typed (see figure 5.3) stretcher from B.M. Industries. The use of an all reflective setup provides a close to chromatic aberration free stretching, which allows for nearly perfect recompression, mainly limited by the spectral bandwidth of the stretcher[45].

5.1.3 The pulse amplification

After the stretcher a Potassium Dideuterium Phosphate (KD*P) Pockels cell is used to reduce the repetition rate to one 1 kHz by rotating the polarization of every 76000th pulse by 90°, allowing that pulse to couple into the regenerative amplifier, where it is used as a seed pulse in another Ti:Sapphire based oscillator. The crystal is pumped with 532 nm light by roughly 29% of the power delivered by a frequency doubled, Q-switched, diode pumped 30 W Nd:YLF laser³ (DM30W, Photonics Industries). After 13 cavity roundtrips the pulse has obtained the amplifiers energy saturation level of roughly 0.5 mJ, and the pulse is therefore coupled out of the regenerative amplifier by another Pockels cell. Prior to sending the pulse towards the multi-pass amplifier, a third fast-switching Pockels cell is employed to temporally clean the pulse, in particular to minimize self-lasing noise of the amplifier.

In the multi-pass amplifier the seed pulse passes a Ti:Sapphire crystal five times in a bow-tie shaped beam path before it is sent on unto the compressor. The crystal in the multi-pass amplifier is cryogenically-cooled to minus 90 degrees. The cooling of the crystal provides several advantages such as increased thermal conductivity, lower thermal expansion coefficient and a decrease in the thermo-optic coefficient [46]. These effects contribute to a reduction of thermal lensing and the probability of thermally induced damages, this allows for stronger optical pumping of the crystal, and thereby increased amount of gain per pass and a higher saturation level. One disadvantage of the cryo-cooling is instabilities caused by vibrations. Vibrational frequencies that can excite mechanical resonances in the optical table is effectively handled by rubber sheets[38], however a residual noise at the compressor frequency of 2 Hz remains in a frequency decomposition of the power stability spectrum[47].

Two pump lasers are used for the multi-pass amplifier: The residual energy of the frequency doubled DM30W laser, but also with light delivered by a frequency doubled, Q-switched, flashlight pumped 20 W Nd:YLF laser (YLF20W B.M. Industries). In principle the multi-pass amplifier supports amplification of pulse energies up till 10 mJ [38], however in order to increase the lifetime of the optical components the amplification is usually limited to 4 mJ. Another aspect of the lower pulse energy is to limit the amount of pulse degradation of the later recompressed pulse caused by self-action effects such as self-phase modulation within the amplifier[48], or generally through the air in the lab.

5.1.4 The compressor

After the multi-pass amplifier the pulse is expanded in a telescope to a FWHM size of 1.6 cm and then sent towards the compressor. The compressor consists of two gratings, each of them similar to the one in the stretcher, and a retroreflector which allows for a second pass. The gratings are placed in a parallel geometry, which causes them to act as negative dispersion filter[26], and thereby recompressing the positively chirped pulse. Figure 5.4 schematically shows that an antiparallel and a parallel grating configuration lead to chirping of the pulse with opposite signs. Thus as discussed in section 3.2 the compressor removes the chirp.

A final webcam behind a slightly transmitting mirror just before the expanding telescope for the compressor provides enhanced beam pointing stability⁴ of the re-

³Neodymium-doped yttrium lithium fluoride.

⁴Stability of the pointing direction of the beam.

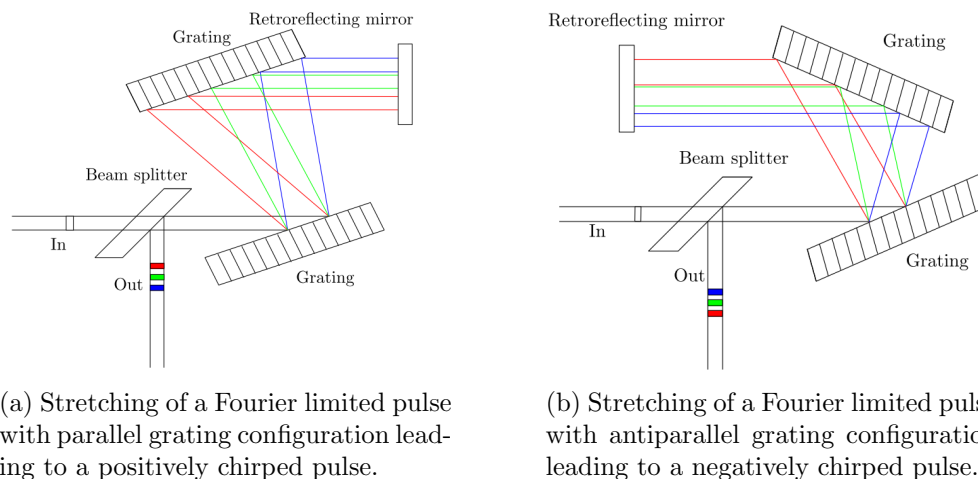


Figure 5.4: Schematic illustration of the different sign of GVD between a parallel grating configuration and an antiparallel configuration.

compressed pulse. The power throughput of the compressor is approximately 75% with a minimum FWHM pulse duration of 34 fs[38].

5.1.5 Beamline for the setup

A silver coated mirror mounted on a holder with a magnetic base plate was used to create a separate beamline for the setup used for the gas cell and hollow capillary experiments. Whenever the laser was used for other things than these experiments the entire mount including the mirror was merely removed. The magnetic base plate provided an inexpensive fast way of switching back to this setup while maintaining the full beam and a reduction in the amount of required realignment.

After the magnetic mounted mirror a series of periscopes and mirrors were placed in order to transport the beam to the experimental setup. In total reflections of 11 silver coated mirrors, each with a reflectance of 800 nm light of roughly 98 %, reduced the pulse energy to roughly 80 % of the compressor output. A 50/50 beam splitter was placed at the setup further reducing the pulse energies to roughly 1.2 mJ. The part of the beam reflected by the beam splitter was used for these experiments; while the transmitted part was used for other experiments.

5.2 The vacuum system

Part of the idea for the project was to construct a simple setup, which is able to efficiently generate low order harmonics, without the requirement of a sophisticated high-vacuum installation. Therefore the work involved the design and construction of a relatively cheap simple vacuum system, which is able to handle the task of generating a sufficient vacuum for low order harmonic conversion. The vacuum chamber described in the following section was therefore designed to be operational only by the use of a regular vacuum pre-pump. The setup is also intended to be mobile, by being easily assembled and disassembled. The chamber was used for the

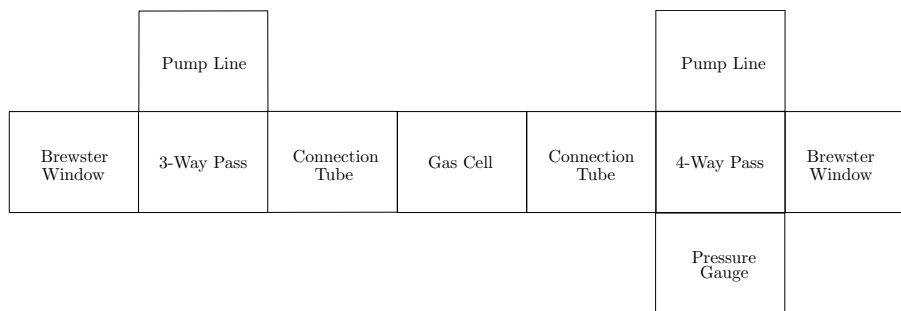


Figure 5.5: Blockdiagram of the vacuum setup.

static gas cell and the capillary experiments, while a different setup (see section 5.4) was used for the generation in a pulsed gas jet.

The focusing optics for the experiments were placed outside the vacuum chamber, so a relatively long chamber was required in order to prevent nonlinear optical effects in the windows.

A block diagram of the vacuum system is sketched in figure 5.5, it consists of a number of interchangeable plexiglas tubes of variable lengths connected with standard KF⁵ vacuum components for two pump-lines connected to the same roughing pump and a pressure gauge. The gas cell for third harmonic generation was placed at the center of the vacuum chamber, while the ends were sealed off by Brewster angled windows. The total length of the chamber was usually between 1.5 m and 2 m, depending on the requirements of conducted experiment.

It was estimated that the setup would be able to withstand an average gas pressure of up to 2 bars. The use of very thin windows to limit dispersion and nonlinear effects was the limiting factor. When turned on the roughing pump was able to vent the vacuum chamber down to 0.3 mbar (measured with a Stinger CVM-211 pressure gauge) within five minutes. After turning off the pump again, the pressure inside the chamber slowly increased to roughly 10 mbar over the course of 24 hours, indicating a sufficient low leak rate.

For obvious reasons the gas cell was removed and replaced with a capillary during the capillary experiments.

5.2.1 The windows

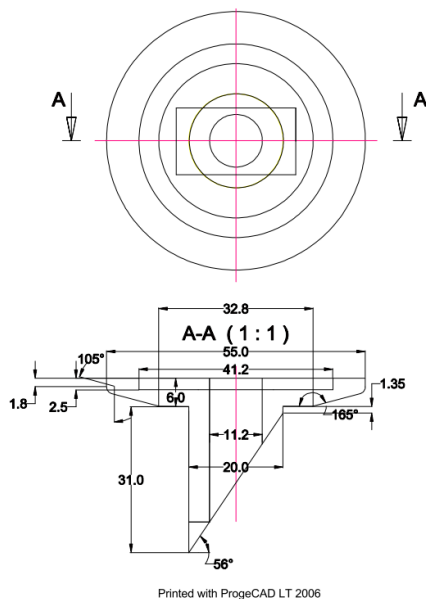
The entrance window consisted of a circular UV grade fused silica⁶ (SiO₂) plate with a diameter of one inch and a thickness of 2 mm. The plate was placed at Brewster angle to minimize reflection⁷ of the incoming beam. A Brewster angled holder with KF40 connection was designed in ProgeCAD and produced by the local workshop. The design is shown in part (a) of figure 5.6, while part (b) shows the final product. The glass plate was simply glued onto the holder leaving a clear aperture of 10 mm.

The exit window was made in a similar way. However, the plate in this case was a rectangular one inch calcium fluoride (CaF₂) plate with a thickness of 0.5 mm. The reason for the different choice of exit window is threefold: First and foremost,

⁵KF is a standardized vacuum connection, which allows for easy assembling with relatively low leakage.

⁶Silica with a metallic impurity of less than 1 part per million.

⁷At Brewster angle the reflectance of p polarized light drops to zero[14].



(a) Design for Brewster window holder.



(b) Brewster window holder.

Figure 5.6: The Brewster cut KF40 connection piece with an inner diameter of 11.2 mm. (a) Shows the design, the upper part shows the transverse profile, while the lower part shows the longitudinal profile. The square on the upper part of the figure shows the position of a rectangular one inch window. (b) Shows a picture of the final product.

the cutoff wavelength of transparency for CaF_2 (~ 140 nm) is shorter than for fused SiO_2 (~ 170 nm) with less dispersion in the deep UV[49, 50]; second, the dispersion of the harmonic light is higher than for the fundamental light, so a thin exit window that minimizes the temporal broadening is required; finally the birefringence of CaF_2 is extremely low for wavelengths longer than 180 nm[51], the CaF_2 window should therefore in practice be polarization maintaining. The two windows were supplied by Eksma Optics.

5.2.2 Mechanical support

The entire setup was supported at the connection tube lines at either end of the setup by a pair of aluminum holders. The holders were each mounted onto a manual 3D-translation stage from Thorlabs, which allowed for micrometer precision in the positioning of the setup. This level of accuracy was especially needed for the capillary experiments, which were required to be well-aligned both in position and angle in order to maximize the coupling into and through the fiber. These holders were also designed in ProgeCAD, and custom-made by the local workshop for this project. A sheet of rubber was used to separate the tubes and the holders in order to minimize mechanical stress on the tubes, whenever the tubes were moved by the translation stages.

5.3 The static gas cell experiments

In the gas cell experiments the light pulse was focused into a gas cell located inside the low-vacuum chamber filled with a static pressure of gas. The cell was placed inside a vacuum chamber in order to minimize distortion effects when the pulses propagate to and from the focus. By limiting these effects the beam maintains a more well-defined profile while being focused, which should be beneficial for the non-linear process of frequency conversion as the intensity is increased at the focal point. Also reabsorption of the generated field is minimized inside a vacuum chamber.

The static pressure gas cell was achieved by allowing a continuous inflow of gas into the cell, while at the same time pumping the vacuum chamber far from it.

A gas cell holder with KF40 connection parts was designed in ProgeCAD. The holder consisted of a 1.88 cm long cylindrical piece, with a 15 mm wide hole in the middle into which the gas cell was mounted. The gas cell was then sealed off from the remaining vacuum chamber by use of rubber rings, which were mashed into the side of the cell by attachable washers. A 6 mm wide hole was drilled in the middle of the holder in order to connect a copper tube with an inner diameter of 2.5 mm. The other end of the copper tube was connected to a valve from Swagelok, allowing it to work as a gas inlet.

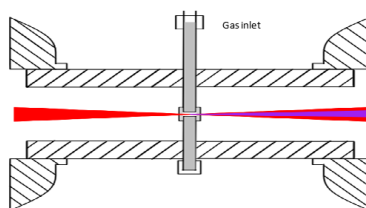


Figure 5.7: The principle of the gas cell. Light at the fundamental frequency of the laser is focused inside a gas cell filled with gas. Due to nonlinear interaction between the gas and the incoming radiation, light oscillating at other frequencies is generated.

The first gas cell consisted of a hollow 3 cm long cylindrical Plexiglas tube with a 2 mm wide hole in the cylinder wall at the middle of the longitudinal direction in order to fill the cell with gas through the inlet. The cylinder was sealed off at the ends by several layers of Teflon tape. The laser was used to *in situ* drill a hole in the tape, allowing the following light pulses to pass through the cell. By drilling the hole with the laser itself the width was minimized as much as possible. The light pulse was focused into the center of the cell by a 75 cm focal length lens, ignoring pulse distorting effects this would lead to a beam width of roughly 0.1 mm at the cell entrance. The cell was then filled with gas pressures between 1 and 4 bar.

Although the laser drilled hole was not larger than the laser beam itself at the respective positions, the gas leak rate was rather high, resulting in high gas consumption and a low pressure ratio between the cell and the chamber.

In order to reduce the gas leakage two possibilities were apparent; either reducing the gas cell size or changing the spot size at the cell wall by using a telescope to reduce the beam size and then focusing it with a significantly longer focal length lens. This would increase the spot size at the focal plane, but at the same time decrease the beam divergence resulting in a smaller beam at the cell wall; the second

possibility was to drastically reduce the cell size. We opted for the second solution. Instead a gas cell was made from one of the connection tubes. A hole was drilled all the way through it and a plastic tube with a 6 mm outer and 4 mm inner diameter was connected. Figure 5.7 schematically show this gas cell. As before the laser was used to drill a hole for itself, while a layer of aluminum foil wrapped around the cell was used to block the less intense part of the beam, and thereby decrease the hole size. The pressure inside the cell was adjusted by a pressure regulator mounted directly on the gas bottle.

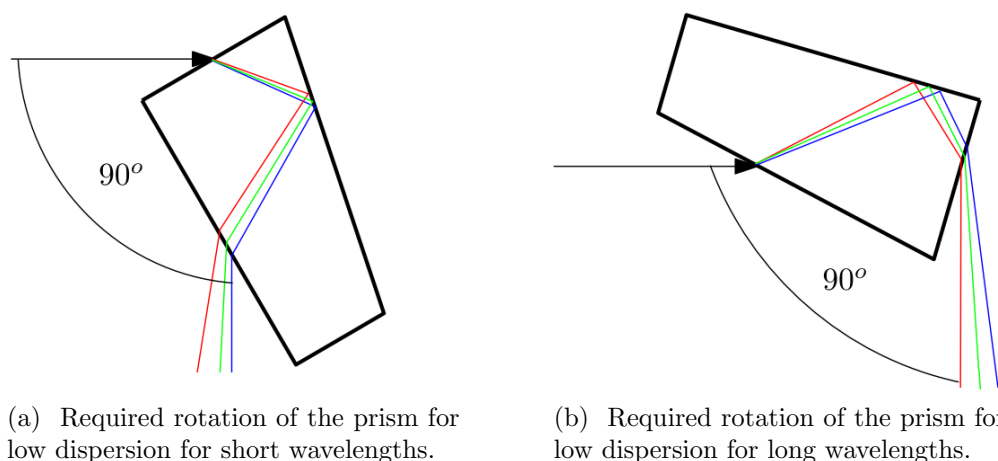


Figure 5.8: The Pellin Broca prism.

Behind the vacuum chamber the combined fundamental and harmonic beam was collimated by a silver coated curved mirror with a focal length of 75 cm. After collimation the fundamental part of the beam was attenuated by the use of a pair of UV graded fused silica mirrors with high reflectivity ($> 99.5\%$) coating for 261-266 nm light at an incidence angle of 45° . The mirrors were rotated such that the light was considered to be p polarized, since the reflectivity at the fundamental frequencies is substantially lower for p polarized light, while the coating still reflects 99% of light with wavelengths between 261 and 266 nm. In order to measure the absolute pulse energy of the third harmonic signal with a very sensitive photodiode silicon based sensor (PD300-UV-193 from Ophir Optronics) further attenuation of the fundamental light are required, since a transition resonance makes the detector more sensitive to infrared light. To improve the signal to noise contrast of the third harmonic beam the use of a Pellin Broca prism was therefore invoked. In this special kind of prism the angle between the input beam and the output beam of a specific wavelength is exactly 90° , while other wavelengths are dispersed into angles deviating slightly from this. As indicated by figure 5.8 it is in principle possible to select which wavelength is emitted at 90° simply by rotating the prism. The advantage of the prism is that it is only weakly dispersive such that the pulse maintains an almost beam-like spatial distribution afterwards. A piece of Schott glass (WG 320), which is opaque for wavelengths below 300 nm, was used to verify that the measured beam only consisted of third harmonic light.

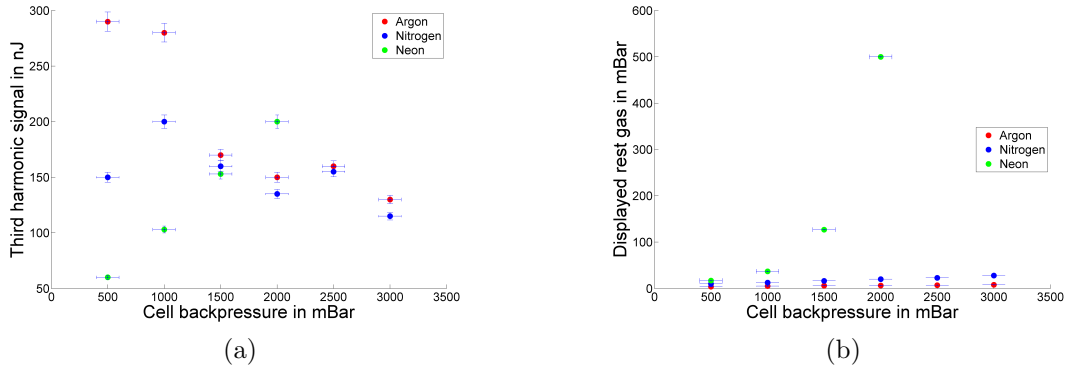


Figure 5.9: The results of the gas cell. (a) The measured amount of third harmonic signal as a function of the backpressure from the gas bottle. (b) The pressure inside the surrounding vacuum chamber as a function of the backpressure.

5.3.1 Results and discussions for the static gas cell

Part (a) of figure 5.9 shows the measured pulse energy as a function of the backpressure from the gas bottle for three different gases; argon, neon and nitrogen. Part (b) of the figure shows the amount of gas which had leaked from the cell into the remaining chamber as a function of applied backpressure. Since the backpressure was merely measured at the gas bottle without further control the pressure was estimated to be within ± 100 mbar of the displayed. For the pulse energy the uncertainty was on the other hand estimated to be that of the detector, which was $\pm 3\%$ for 266 nm light.

A pressure dependent third harmonic signal is clearly apparent in all gases. For argon and nitrogen the signal features two local maxima. The conversion in argon seems to be slightly higher, which is well-explained by the higher nonlinearity of argon compared to that of nitrogen. Choosing backpressures below 500 mbar was not possible with the available pressure reducer. However, when the gas bottle was closed, while leaving the pump still venting the chamber, such that the pressure inside the gas cell decreased below 0.5 bars the signal rose to a peak value of 420 nJ for argon and 300 nJ for nitrogen before dropping to 0 nJ once the chamber was completely vented. Since the pressure for these two values was not measured these points were omitted in the figure. However, the peak indicated that the optimum generation pressure was somewhere in the regime of 0 to 0.5 bar for either gases.

When compared with the simulated curve for direct third harmonic generation in argon shown in 4.6 the measured oscillating result clearly differed from the calculated oscillations - both in period and the maximum signal envelope. There can be many reasons for these deviations, since the code is a simple time-independent 1-D code, which only considered the on axis response.

In particular the code did not take into account electric field alterations caused by the interplay between self-focusing and defocusing effects of the pulse close to the geometrical focus inside the gas cell. In the experiments the interplay led to a formation of a self-guiding filament for the pulse. For 1 bar of argon the filament ranged from roughly 2 cm before the cell to 1 cm after, such that it had a total length of around 3.6 cm. Within the filament the pulse continuously self-focuses and defocuses, which leads to a more or less constant intensity around the geometrical

focus. The self-focusing is predominately caused by the optical Kerr effect, while the defocusing is caused by plasma diffraction. The filament ends when the pulse power has decreased sufficiently such that the diffraction caused by the plasma eventually overtakes the self-focusing.

As the code did not take into account depletion of neither the fundamental field nor the third harmonic, caused by absorption or by conversion into other frequencies, it cannot be applied for THG in dense gases, where these effects becomes stronger. Also, since higher gas concentration increases the probability of ionization, the critical free electron density occurs at lower intensities for dense gases. The decrease in obtainable intensity means, that the effects of the nonlinear refractive index stops scaling as according to the simple theory. As a bare minimum one in principle needs to simultaneously solve the propagation of the fundamental electric field envelope between each step of propagation for the third harmonic field envelope (equation (4.1) on page 21), to accurately determine the generated third harmonic signal. This would require a considerable time-consuming overhaul of the code, time that would probably be better spent on deriving a proper propagation code from scratch. Nevertheless, the simulations did predict pressure dependent phase-matching oscillations of the correct order of magnitude.

For the generation in neon the process was clearly still fairly phase matched for all data points, since the generated signal was monotonically increasing for the entire measurement.

During the capillary experiments a high pressure of argon was needed inside the chamber, so the pump was turned off, while the pressure regulator was set to 1 bar. However, the pressure gauge still displayed a pressure of around 37 mbar. Initially this led us to believe that the pressure gauge was malfunctioning. However, a short consultation with the manual revealed that the gauge was in fact a Pirani gauge. In a Pirani gauge a metallic wire is connected to an electrical circuit, whenever a molecule or an atom hits the wire energy is dissipated from the wire. The energy dissipated from the wire causes it to cool, which changes the conductivity. The conductivity is then interpreted as a given pressure, since the rate of collision is dependent on pressure. Since the amount of dissipated energy per collision depends on the thermal conductivity of the gas, the readout is dependent on gas type. Below roughly 1 mbar the gauge response is linear and the gas type dependence is noncritical, such that gauge displays more or less the correct pressure for all gases. However, above 1 mbar the gauge response becomes nonlinear due to cascaded processes, so the displayed gas pressure becomes highly gas type dependent. The gauge had only been calibrated for nitrogen by the manufacturer, while the manual provided a set of data points for conversion into other gases.

Part (a) figure 5.10 shows the tabulated conversion values for neon provided by the manufacturer, along with a nonlinear fit in order to provide conversion for other pressures. Part (b) of the same figure shows the conversion for argon. While part (c) shows the estimated residual pressure in the vacuum chamber as a function of the backpressure, after the nonlinearity of response for the pressure gauge had been taking into account. Uncertainty bars have been omitted for the adjusted pressures, because of the difficulties in determining them properly. In particular, the pressures for argon are very imprecise.

Several ways of reducing the gas leakage from the gas cell was investigated throughout the experimental work. Among these the most prominent try was to construct a gas cell consisting of a 3 cm long solid rod with an outer diameter of

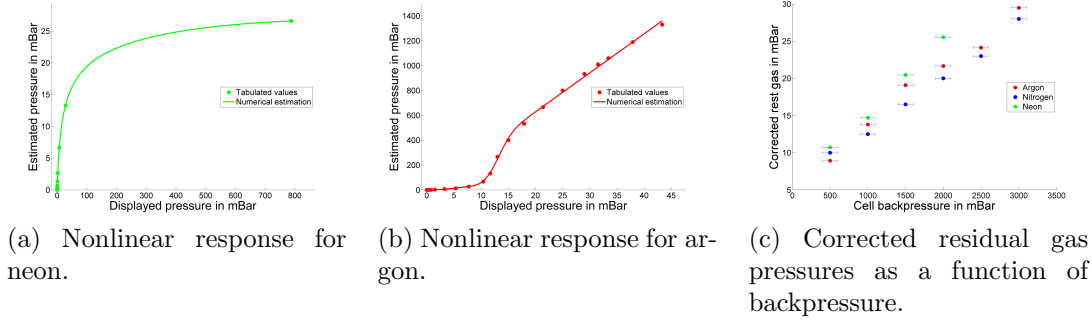


Figure 5.10: (a) Numerically estimation for the nonlinear response curve for neon of the gauge. (b) Numerically estimation for the nonlinear response curve for argon of the gauge. (c) The corrected residual gas pressure as a function of the backpressure from the gas bottle for argon, neon and nitrogen.

15 mm and a 1 mm hole in the middle. A 4 cm long hollow capillary with an inner diameter of $250\ \mu\text{m}$ was glued into this hole. A roughly $70\ \mu\text{m}$ wide hole through the cladding of the capillary was drilled with the laser prior to gluing it into the rod. This gas cell was mounted into the mount described earlier. Part (a) of figure 5.11 shows a side view of the capillary. Part (b) and (c) of the same figure respectively show the third harmonic signal and the leakage into the vacuum chamber as functions of the backpressure for argon and nitrogen.

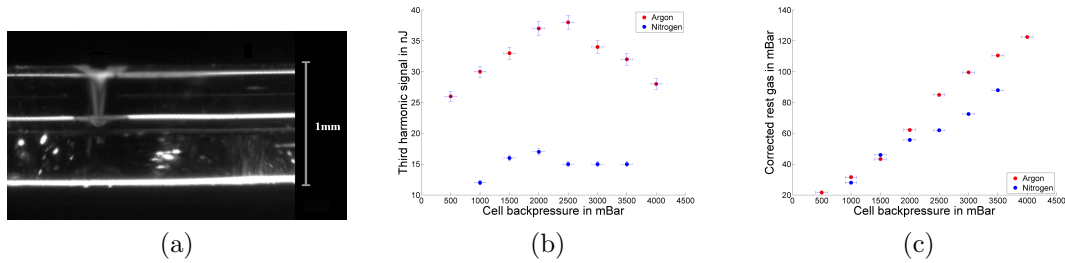


Figure 5.11: Results for an alternative gas cell. (a) Cross-sectional view of a capillary with a hole drilled through the cladding, this capillary led the basis for the alternative cell. (b) The third harmonic signal as a function of backpressure. (c) The adjusted gas leakage as a function of backpressure.

One notices that the gas leak rate were much higher than before, which clearly indicates that the entrance hole for plastic tube based gas cell was substantially narrower than $250\ \mu\text{m}$. One also notices that the overall throughput of third harmonic signal is reduced almost tenfold. The reduction in throughput was probably related to the higher gas leakage, which limited the focusing. However, the main reason for the decreased signal was probably, that the holder supporting the capillary was lacking angular alignment. Since time was limited coupling into the waveguide was not optimized and a large part of the fundamental beam was not transmitted. The therefore less intense generating field led to a lower amount of third harmonic generated signal.

5.4 The pulsed gas jet experiments

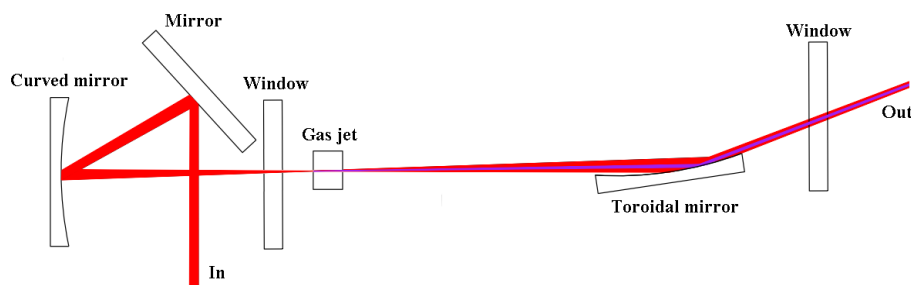


Figure 5.12: The setup for the pulsed gas jet experiments.

The second part of the experimental work involved a pulsed gas jet for low order harmonic generation. Since such a jet already existed in the lab as part of a high harmonic generation setup (shown in figure 5.12), this setup was therefore used for this part.

A spherical mirror with a focal length of 50 cm was used to focus the IR light pulses into the pulsed gas jet located inside a high vacuum chamber (10^{-5} - 10^{-6} mbar). The jet consisted of a 6 mm long aluminum block with a 1 mm wide hole through the center. Another hole from the backside of the block connected the 1 mm hole with a high gas density chamber. A piezoelectric valve was used in between the thin nozzle and the high gas density chamber.

The cell was mounted on a motorized 3-D translation stage, in order to optimize the coupling of light into the jet. The valve was opened at a repetition rate of 1 kHz synchronized with the laser by applying voltage to the piezoelectric material, which when expanded sufficiently squeezed the sealing rubber ring such that gas could leak from the back chamber into the cell, and thereby creating a gas jet[52].

60 cm after the jet the beam was refocused by a toroidal mirror with 30 cm focal length. The exit CaF_2 window for the chamber was located right behind the toroidal mirror, so the focal plane of the refocused beam was well outside the chamber. The converging third harmonic pulse was separated from the fundamental pulse right after the vacuum chamber by a pair of band-pass mirrors and a Pellin Broca prism in a similar way as in the part with a static gas cell.

In order to generate extreme ultraviolet (XUV) light through the process of high harmonic generation[4, 5], the gas jet is normally operated with at relatively low voltage, such that residual gas in the chamber is in the range of $3\text{-}4 \cdot 10^{-3}$ mbar, which corresponds to a pressure in the jet in the range of a couple of tens of mbar.

For these experiments with THG in a pulsed jet it was initially tested whether it would be beneficial to turn off the turbo pumps and operate the jet at a considerably higher pressure. However, even when the rest pressure in the chamber was merely 10^{-1} mbar a strong filament was generated. The generated third harmonic signal was greatly reduced within the filament, due to strong absorption and the tight focusing. The turbo pumps were therefore turned back on, and the jet operated at pressures close to the ones used for high harmonic generation. The simultaneously generated XUV light was a non-issue for the detection, due to the short attenuation length of XUV light in the window.

5.4.1 Results and discussions

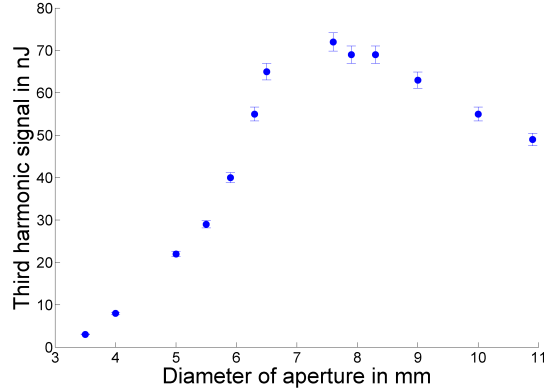


Figure 5.13: Optimization of aperture size for the third harmonic generation in argon, for a rest gas pressure of $5 \cdot 10^{-3}$ mbar.

In order to maximize the third harmonic output the following parameters were all optimized; pulse compression, pulse energy, delay between the gas valve and light pulse, backing pressure of the gas bottle, and the overall alignment. As an example of this optimization of pulse energies are shown in figure 5.13 at a backpressure of 5 bar and a rest gas pressure of $5 \cdot 10^{-3}$ mbar. The pulse energy was adjusted by aluminum apertures of various sizes.

Figure 5.14 shows the pressure dependence of THG for conditions which were optimized for third harmonic generation for a rest gas pressure of $5 \cdot 10^{-3}$ mbar. The signal clearly scales almost quadratically with the rest gas pressure, and thus with the generation pressure, under the reasonable assumption that the pressure inside the jet is linearly proportional to the rest gas pressure. This corresponds to the case, where the phase mismatch between the fundamental light and the generated signal is nearly the same for all the different pressures, which causes the phase integral given in (2.12) to be approximately constant. The measurement was stopped at 10^{-2} mbar in order to prevent overloading of the turbo pump, although no limitations of the signal caused by phase-matching had been observed.

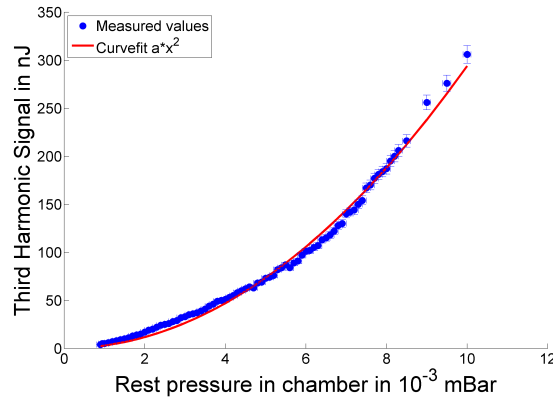


Figure 5.14: Measurement of the pressure dependence on the third harmonic generation in a gas jet, along with a quadratic fit.

5.5 The hollow capillary experiments

The final part of the experimental work for this thesis concentrated upon phase-matched difference frequency generation of two-color fields inside a hollow capillary. The hollow capillary was made from a 1 m long fused silica glass tube, with a hollow core with a diameter of $250\ \mu\text{m}$, the outer diameter of the tube was 1 mm.

The capillary was placed in a V-grooved mount inside the vacuum chamber described in section 5.2. The chamber was vented and then refilled with various gases. Unlike in the gas cell experiments the roughing pump for the setup was turned off throughout these experiments, such that the entire capillary was kept at a static pressure.

This experimental setup involved reflections from a substantial higher number of surfaces, than the gas cell experiments, so the 50/50 beam splitter in front of the setup was replaced with a mirror in order to increase the power.

5.5.1 The two-color interferometer

The two-color field consisted of the fundamental light pulses delivered by the laser, and frequency doubled light pulses. The roughly 0.1 mJ frequency doubled pulses were generated in a 0.7 mm thick KDP crystal using the entire 2.4 mJ IR pulse, which corresponds to a conversion efficiency of roughly 4%. The generated second harmonic pulse should have a duration similar to that of the IR pulse, since the KDP crystal was shorter than the phase-matching length for SHG, and comparable to the theoretical walk-off length⁸. The spectral FWHM width of the second harmonic was roughly 6 nm, which for a Gaussian pulse with a central wavelength of 400 nm would correspond to a Fourier limited duration of roughly 40 fs. The SHG pulse was likely not Fourier limited, but the duration was properly still in the range of tens of femtoseconds.

Due to different group velocities of these two extremely short pulses, a fine control of the timing between them was necessary in order for them to overlay in time at the capillary. To handle this task a two-color interferometer was employed.

Figure 5.15 shows a schematic overview of the interferometer used for these experiments. A dichroic mirror was used to generate the two arms of the interferometer by transmitting the fundamental frequency light, while light at the second harmonic frequency was reflected by the mirror. The length of the blue arm was controlled by a translation stage mounted vertically. The translation stage could mechanically be controlled by a micrometer screw with a precession of $1\ \mu\text{m}$, while a piezomotor with a travel range of $20\ \mu\text{m}$ provided an additional fine control of the path length on the nanometer scale. A periscope in the blue arm was used to turn the polarization by 90° , such that once the two beams were recombined by a second beam splitter they had parallel polarizations. A half-wave plate and a polarizer with an extinction ratio of 50:1 in the IR path were used to precisely control the strength of the IR light transmitted through the interferometer. The sub-micrometer precession in the path length differences between the two pulses provided a sub-cycle control of the temporal alignment for the two pulses.

⁸The propagation distance inside KDP for which the SHG light generated at the start of the crystal still overlays in time with the fundamental pulse[26].

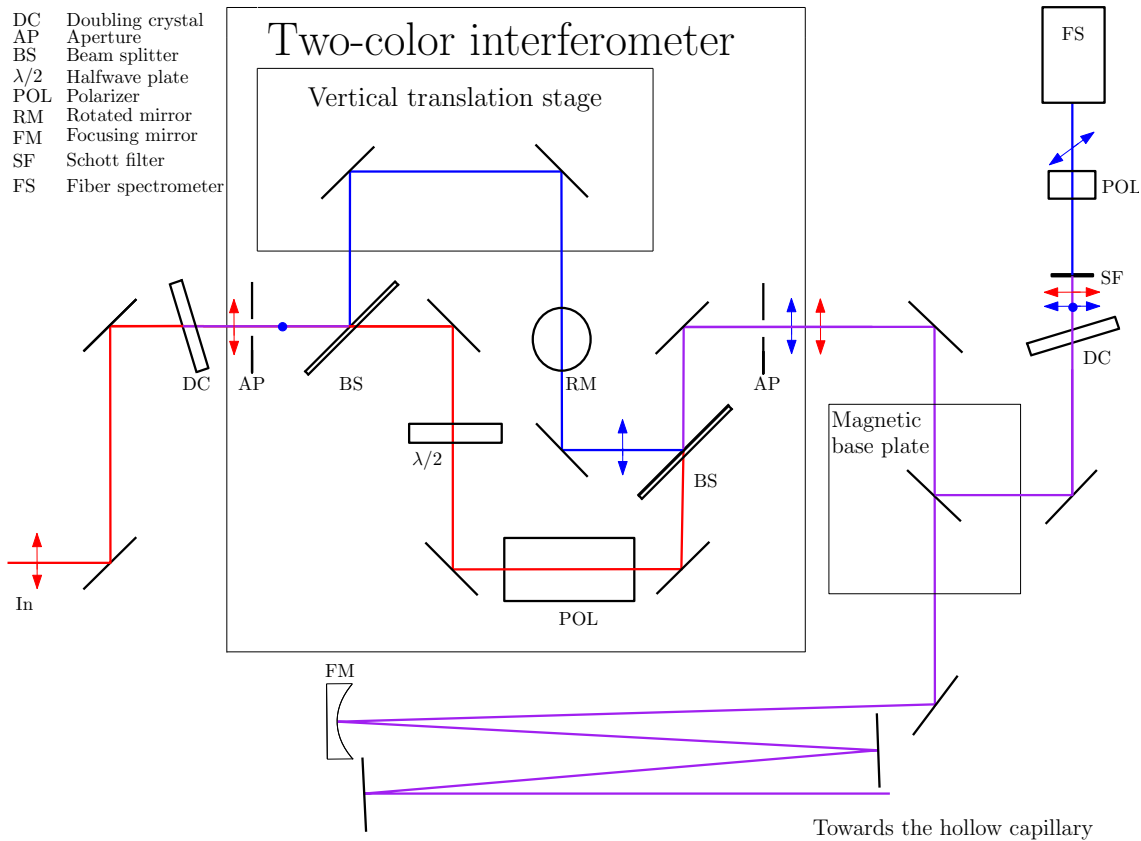


Figure 5.15: Overview of the two-color interferometer.

After spatial alignment of the interferometer rough temporal alignment between the two pulses were found by frequency doubling the IR pulse in a second $50 \mu\text{m}$ thin KDP crystal after the interferometer, and then looking for interference between the two blue pulses. The IR light was removed by a Schott glass filter, while a polarizer rotated at 45° forced the two blue pulses to have the same polarization. The time overlay was then observed by looking for spectral fringes of the two pulses with a fiber coupled spectrometer. Once this was found, the time delay between the two co-propagating blue pulses was optimized by adjusting the fringe pattern between them. Figure 5.16 shows the optimized interference pattern between the two blue pulses. The time delay between the IR and SHG pulses from the interferometer were very slightly shifted from the delay between the two blue pulses, due to the finite length of the second doubling crystal. However, this small deviation in the timing inside the capillary was easily handled by the delay stage of the interferometer.

The throughput of the interferometer was 1.42 mJ for the red arm, and 0.08mJ for the blue arm. After the interferometer a focusing mirror with focal length of 1 m and four additional folding mirrors, which were used to minimize spherical aberrations of the focused beam, reduced the fundamental pulse energy to roughly 1.2 mJ at the entrance window for the vacuum chamber.

It was initially investigated if it would be beneficial to insert a Galilean telescope[20] in front of the first doubling crystal in order to increase the amount of generated blue light. However, this was dropped again, since a demagnification of merely 2 times, led to a strong pulse degradation of the IR pulses, caused by an increase in the nonlinear interactions of the more intense beam within the various

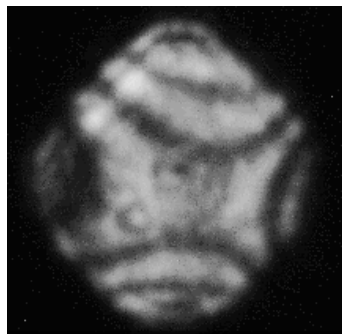


Figure 5.16: Interference pattern between the two SHG pulses.

materials and air.

5.5.2 Aligning the hollow capillary

Aligning a hollow capillary is a non-trivial task in itself. The capillary was pre-aligned from the back end with an ultra-stable helium neon (HeNe) laser. Once in-coupling of the light from the helium neon laser was optimized, the mirrors between the interferometer and the normal entrance to the vacuum chamber were aligned such that the HeNe beam was transmitted through the interferometer. An additional aperture was inserted just in front of the vacuum chamber to help define the optimum beam path. The HeNe laser was thereafter removed and the femtosecond laser was sent towards the setup. The focal length of the focusing mirror was selected such that the beam waist of the focused IR beam matched the theoretically optimum size for coupling into the fundamental electric field mode of the capillary. Since the focusing for both beams were conducted with the same mirror, the blue beam was too small for optimum coupling into the fundamental mode. This meant that higher order modes were excited by the blue. It also meant that coupling of the blue beam was easier. The procedure for coupling was therefore to first optimize the coupling of the blue beam with the two alignment mirrors after the focusing mirror, and then using the last two mirrors in the red arm of the interferometer to optimize coupling of the IR beam. Figure 5.17 shows the far field modes of the transmitted beams for the IR beam and the beam from the HeNe laser. The throughput of the capillary at a vacuum pressure of 10^{-1} mbar was 0.54 mJ for the IR beam, and 0.02 mJ for the second harmonic beam. At one bar of argon or air the optimized IR throughput had decreased to roughly 0.4 mJ. The blue beam was attenuated a bit more due to higher reflections of the entrance and exit windows of the chamber, since they were placed in Brewster angle for the IR beam which is a different angle for than the Brewster angle for the 400 nm beam. Also the fact, that the higher order modes have a higher attenuation coefficient inside the fiber[34] played an important role in the stronger attenuation of the blue beam.

5.5.3 Results and discussions

The signal was detected in two ways; the first method was similar to the previous experiments, where the beam was collimated by a curved silver mirror, and then using a pair of band-pass mirrors and a Pellin Broca prism in order to measure the

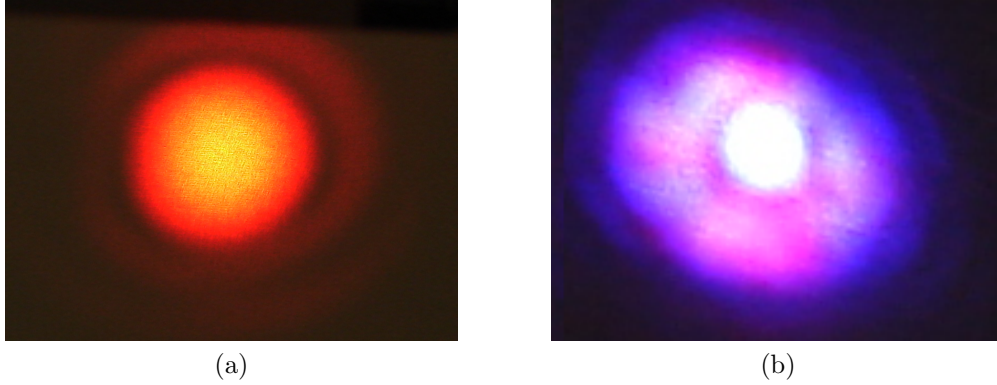


Figure 5.17: (a) The far field transversal beam profile of the helium neon laser beam transmitted through the fiber. (b) The far field transversal beam profile of the IR beam transmitted through the fiber.

absolute strength of the third harmonic signal; the second method was to block the entire beam directly after the chambers exit window, and then record the entire reflected spectrum with a fiber spectrometer (AvaSpec-3648) with a solarization⁹ resistant fiber (Avantes FC-UV100-2-SR). The spectrometer had a spectral range of 190 nm to 1100 nm with a resolution of 1.4 nm.

The temporal overlap inside the capillary was found by filling the capillary with atmospheric pressure of air, sending in the blue and IR beams, and changing the delay of the blue pulse, while carefully watching the output pulses for obvious changes. Figure 5.18 shows how the blue pulse was spectrally changed by propagation inside the capillary as a function of the delay between the two pulses. A spectral alteration of the blue pulses was observable at four different delays. The first and also strongest shift corresponds to the temporal overlap of the blue and red pulse. The intense red pulse causes the blue pulse to feel a strongly time-dependent refractive index, which leads to a spectral broadening and shift of the blue pulse.

The time-dependent refractive index is caused by interplay between several effects, such as cross-phase modulation¹⁰, the generation of free electrons and the excitation of rotational wave-packets.

The cross-phase modulation leads to a blue-shift or a red-shift depending on whether the blue pulse coincides with the rising or the falling slope of the IR pulse. The blue pulse is additionally blue-shifted by the creation of free electrons, which is likewise mainly driven by the intense IR pulse.

The main reason behind the apparent long cross-correlation signal, were however probably due to the formation of rotational wave-packets. Prior to the IR pulse the air is isotropic; however the intense IR causes the molecules to spatially align breaking the isotropy of the gas. Molecular alignment can either reduce or increase the refractive index depending on the polarization of the light. Quantum mechanically the alignment is described by the excitation of a number of rotational states $|J\rangle$.

⁹Long term UV transmission of normal silica based fibers is heavily decreased by the formation of strongly UV absorbing intrinsic defects inside the silica core, these so-called color centers are centered around 210 nm and 265 nm[53]. This effect is termed solarization.

¹⁰The two-color equivalent of self-phase modulation, where a time-dependent intense beam causes a spectral change in weaker beam through the optical Kerr effect.

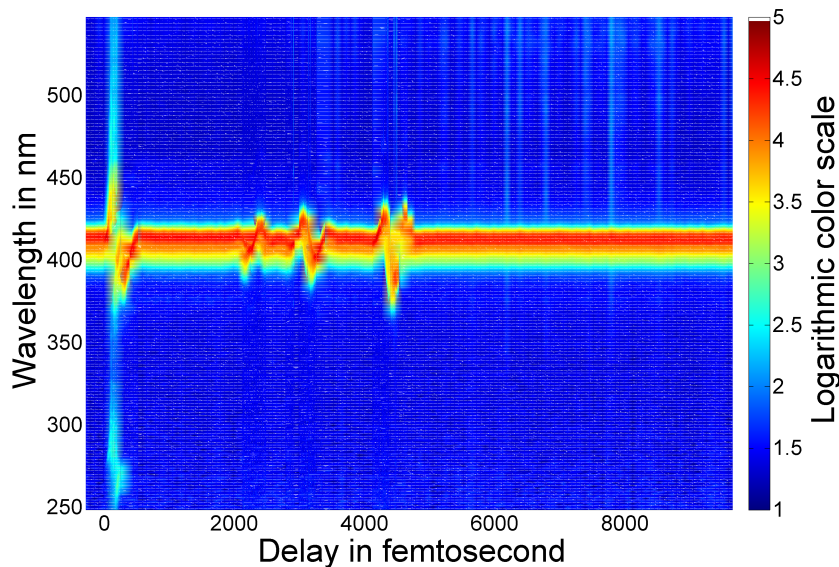


Figure 5.18: Spectral alterations of the frequency of the second harmonic light coming out of a capillary as a function of the delay between the IR and SHG pulses sent into the capillary.

These rotational states have different angular frequencies ω_J given by[54]:

$$\omega_J = \frac{1}{2}J(J+1)\omega_1, \quad (5.1)$$

where ω_1 is the angular frequency of the lowest order excited state. Since the various rotational states have different angular frequencies they dephase. The dephasing occurs within a couple of hundreds of femtoseconds, after which the rotational alignment is lost.

Unless additional decoherence effects have happened all states rephase again at a certain time and the alignment is regained. The realignment is called rotational revival, and happens when the phase of the fundamental state has changed by a integer number of 2π . For nitrogen and oxygen this happens about 8.4 ps and 11.2 ps after the aligning pulse respectively[54]. One can also have partial revival for a number of rotational states at certain fractions of the full revival time.

The delayed spectral shifts of the blue were in good agreement with precisely measured quarter-cycle revival times for nitrogen (~ 2 ps) and oxygen (~ 3 ps), as well as half-cycle revival in nitrogen (~ 4 ps).

The mean free path of air is roughly 64 nm at atmospheric pressure¹¹. If the molecules had been moving at the normal speed of sound they would have moved a considerably shorter distance (about 2 nm in 6 ps) and decoherence due to collisions would not be an issue. However, since the gas also was heated by the intense electric field their velocities were likely several orders of magnitude higher than their normal speed. The thereby higher collision rate would significantly decrease the coherence time, and explain the lack of spectral changes in the blue beam at the theoretical full cycle revival and later.

¹¹Taken from [55].

The interpretation that the latter spectral shifts were due rotational revival were further supported by the lack of similar delayed shifts in the atomic gases of argon and neon, while the first peak was still observable, however substantially narrower.

After the temporal overlap was found for air, the chamber was evacuated and refilled with the desired pressure of argon; the position of the overlap was slightly shifted with respect to the air overlap, due to the small difference for the various group velocities in air and argon. In order to decrease the uncertainty in the pressure for argon, the previously used Pirani pressure gauge was replaced by a regular gas type independent Diaphragm gauge (ASG-2000-NW16). This type of gauge measures the kinematic force exerted by the gas, and is therefore gas type independent.

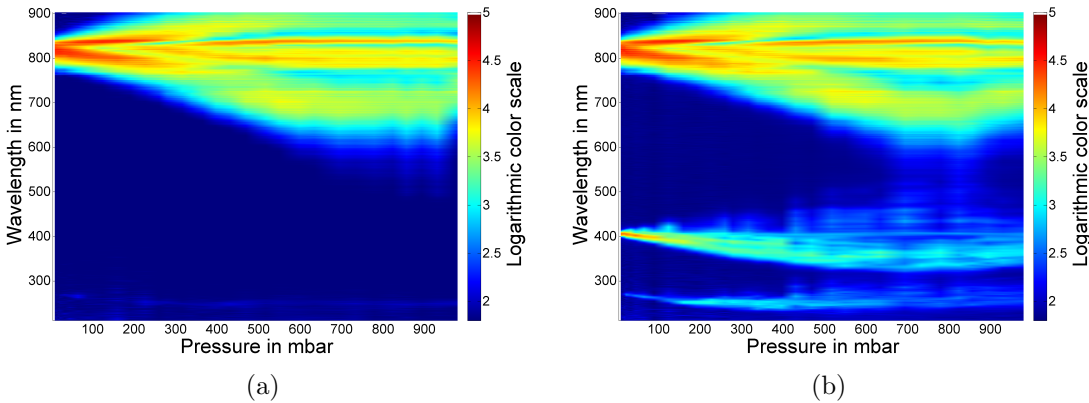


Figure 5.19: (a) Full spectrum as a function of pressure without the blue pulse. (b) Full spectrum as a function of pressure with the blue pulse.

Part (a) of figure 5.19 illustrates how the spectrum of the light transmitted through the capillary depends on pressure when only the IR pulse was sent towards the capillary. The total throughput was optimized each time the pressure was changed; in particular the IR beam often required spatial realignment to optimize the coupling. In good agreement with usual measurements of ultrashort pulse propagation inside hollow capillaries [56, 57], the IR pulse was significantly spectrally broadened. The spectral broadening of the IR pulse was caused by interplay between similar nonlinear effects¹² which led to a broadening of the blue pulse described above, with the obvious exception that molecular alignment did not play a role in this case, since argon is an atomic gas. The broadening was more pronounced at higher pressure, due to increased nonlinearities.

A weak third harmonic generated signal was also visible at all pressures. The THG signal was slightly blue-shifted at higher pressures likely, due to a higher concentration of free electrons.

Part (b) of the same figure shows the transmitted spectrum for the same pressures with both the IR and the blue pulse present. As expected by phase-matching considerations the generation of deep UV light was greatly enhanced by the presence of a 2ω field. By adding the blue beam an additional path to 3ω light was added, namely the DFG process: $2\omega + 2\omega - \omega \rightarrow 3\omega$. The generated signal was

¹²In this case mainly self-phase modulation and generation of free electrons.

centered around 260 nm at low pressures, while higher pressures caused it to be further blue-shifted simultaneously with the shift of the blue. An optimum conversion pressure is obtained between 200 and 500 mbar, while the conversion was limited at higher pressures by the depletion of parts of the blue and IR beams, which were phase-matched for UV generation.

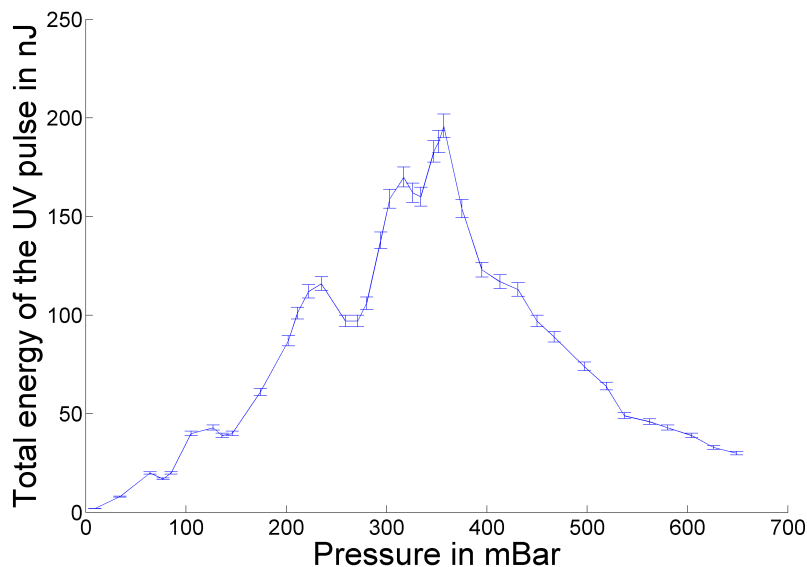


Figure 5.20: The measured UV signal after removal of the IR and SH signal by the band-pass mirror and prism.

Figure 5.20 shows the absolute energy measurements of the UV radiation after separation of the blue and the IR pulses with the prism and the band-pass mirrors. As the spectrum in part (b) of 5.19 shows, is the generated signal both significantly broadened and slightly blue-shifted. This probably led to a decrease in the measured pulse energy compared to the real pulse energy, simply due to the relative narrow bandwidth of the separation mirrors.

The measurement in figure 5.20 shows four different locally optimized generation pressures located around 120, 240, 320 and 360 mbar respectively. These closely spaced generation pressures, could correspond to phase-matched generation from the fundamental mode of the IR beam and capillary modes of different orders for the multi-moded blue beam. It was not possible to determine the mode of the generated beam in a simple way, since a significant amount of blue light was reflected by the band-pass mirrors. The blue beam was therefore not filtered away before the prism, which distorted the beam quality.

Figure 5.21 demonstrates the tunability of the transmitted spectrum. The figure shows how the strength of the IR beam affects the transmitted spectrum for two distinct blue pulse strengths, each measured at three different pressures. As previously described the IR beam was attenuated by rotating the half-waveplate in the red arm of the interferometer. The input pulse energy for each data point was not measured directly, but merely estimated by observing the strength of transmitted IR pulse. The half-waveplate was rotated by hand over a range which corresponded to a polarization change of 180° for each measurement. Since the rotation was done manually the data points were not equidistantly spaced.

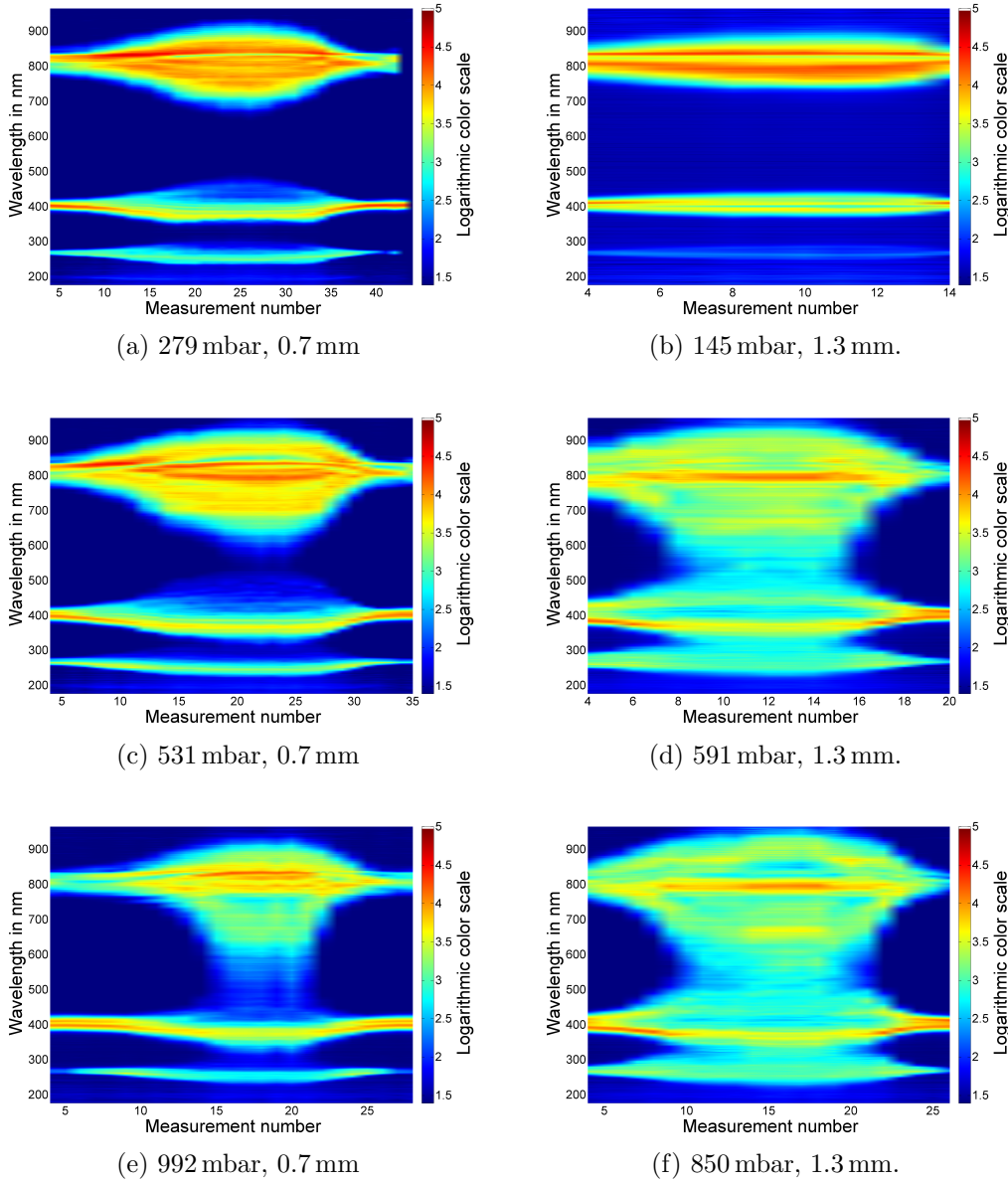


Figure 5.21: Output spectrum from the capillary as a function of the intensity of the input IR field measured at three distinct pressures for two different KDP crystals with respective thicknesses of 0.7 mm and 1.3 mm.

In parts (b), (d) and (f) of the figure the strength of the blue pulse was increased by replacing the 0.7 mm thin KDP frequency-doubling crystal in front of the interferometer by a slightly thicker one (1.3 mm). The thicker crystal allowed for generation of blue pulses with energies up till $20 \mu\text{J}$, at the cost of longer and spectrally narrower input blue pulses. The coupling efficiency of the blue pulse remained the same, so $4 \mu\text{J}$ pulses were transmitted through the capillary.

At low IR intensities the spectral broadening faded in all cases, which led to a generation narrow bandwidth UV radiation usually centered around 270 nm. Increasing the IR intensity resulted in a blue-shift and spectral broadening of all pulses inside the capillary, which clearly supports the interpretation that the IR pulse was

the driving force for these nonlinear effects. White light generation covering the entire range of the spectrometer was obtained with the thick crystal at high gas pressures.

Figure 5.22 shows an enlargement of the spectral range from 190 nm to 450 nm for part (a) figure 5.21. This measurement shows evidence of not only third harmonic generation, but also signs of higher order harmonics by showing a weak fourth harmonic signal. The fourth harmonic frequency light was likely caused by cascaded nonlinearities, where the 3ω light is further upconverted through difference frequency mixing with the other fields. The third-order processes which can lead to 4ω light is:

$$\omega + \omega + 2\omega \rightarrow 4\omega, \quad 3\omega + 3\omega - 2\omega \rightarrow 4\omega, \quad 3\omega + 2\omega - \omega \rightarrow 4\omega. \quad (5.2)$$

Shorter wavelengths were likely to also be generated; however the spectrometer did not support a measurement of these. Using a thin doubling crystal clearly provides more controllability of the output, while a thicker one provides a stronger output. Using the thick crystal likely also causes the generated signal to be more chirped, increasing the requirement for temporal recompression. However the duration of the generated pulses was not measured in the presented work.

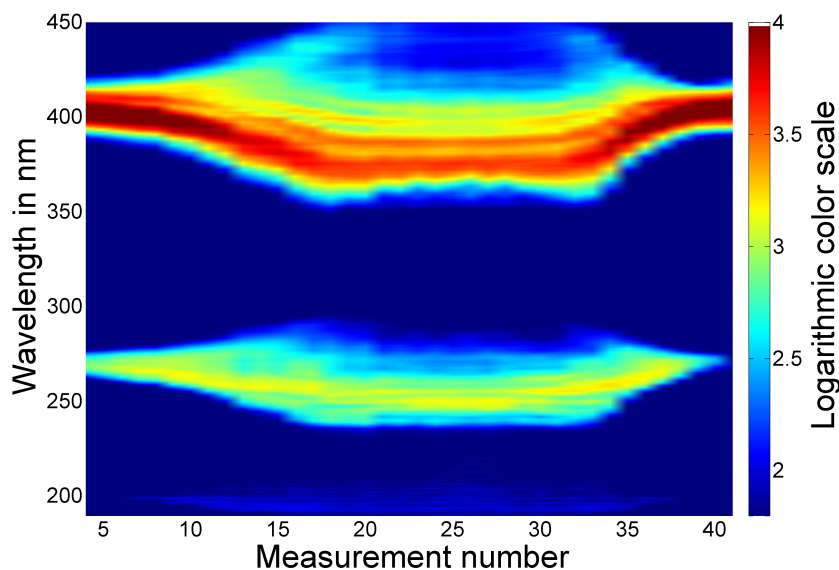


Figure 5.22: Zoom of figure 5.21 (a) to illustrate the IR intensity dependent output spectrum for 190 nm to 450 nm.

CONCLUSIONS AND OUTLOOK

The development in Attosecond Physics has been immense in the last decade. Considerable advances in laser technology around the turn of the century along with discovery of high harmonic generation in the late 1980's created this new branch of physics. These technologies, which allowed for diffraction-limited few-cycle near infrared pulses and extreme ultraviolet light with sub-femtosecond duration, has recently pushed the time-resolution in the study of atomic processes towards their natural unit of time¹[58]. The aim of this thesis was to add deep ultraviolet light to the attosecond technology toolbox, in order to enable single photon attosecond-resolved studies of surfaces and chemical processes.

The thesis was a divided into two parts: A theoretical investigation of the possibilities of generating DUV light by frequency upconversion of ultrashort pulses delivered by a Ti:Sapphire laser, and an experimental part involving the experimental realizations of the theoretical ideas.

The theoretical part concentrated on the aspects of phase-matching. A numerical model was derived, which allowed for studies of how various parameters influence the phase-matching conditions. The code was applied to the simple case of third harmonic generation in a gas cell. These simulations revealed that optimum generation conditions would likely be obtained in a high pressure loose focusing scheme, where the phase-matching conditions should be optimized by fine-adjusting the pressure.

In the experimental part four experiments were designed, in order to evaluate the different methods of generating deep ultraviolet light. The simplest solution for generation third harmonic light, which involved focusing the laser into a static pressure gas cell, showed the highest output with measured pulse energies as high as 420 nJ. The generated pulse was likely significantly higher, since prior to the energy measurements the pulse was recollimated by a silver coated mirror, reflected by a pair of band-pass mirrors, and finally dispersed by a prism in order to separate the fundamental frequencies. The normal reflectivity of silver mirrors in the deep ultraviolet is around 25%, so the total energy of the third harmonic pulses was estimated to be above 2 μ J. On the downside, the method lacked durability and reproducibility. The entrance and exit holes of the gas cell, which were drilled *in situ* by the laser itself, were at high cell pressures expanded severely within minutes. The expanded holes led to a greatly increased gas leakage into the surrounding vacuum chamber, which limited the generated third harmonic signal.

¹The atomic unit of time.

The second method involved using a pulsed gas jet rather than a steady-state gas cell. The technique demonstrated promising results, with measured pulse energies around 300 nJ, without showing any signs of limitations caused by phase-matching issues. The method provided clear advantages of reproducibility over the static high pressure gas cell, while maintaining similar conversion efficiencies. The setup used for this part, was built with the generation of high harmonic pulses in mind, which are efficiently generated at jet pressures around 20 mbar. So the setup was therefore not capable of handling the high pressures involved in efficient third harmonic generation, which limited the highest possible generation pressure prior to phase-matching limitations. Further development of this method would therefore involve the design of a setup, which could support higher pressures in the jet, for example by implementing a differential pumping scheme.

The third and fourth methods were based on hollow capillary schemes. The third method was based on direct third harmonic generation inside a hollow capillary, while the fourth method involved phase-matched difference frequency generation of two-color fields as a pathway to deep ultraviolet light. The two-color field consisted of fundamental frequency pulses delivered by the laser, and frequency doubled pulses. The experimental complexity of dispersion of two-colored fields was handled by the employment of an existing two-color interferometer, which was taken apart and rebuilt to fit our requirements. The two-color interferometer provided a way of obtaining spatial and temporal alignment between the two light pulses inside the capillary.

As evident from figure 5.19 generation of ultraviolet radiation in a capillary strongly benefits from the usage of two-color fields. The two-color scheme increased the deep ultraviolet more than ten-fold, even though the added blue field was ten times weaker than the infrared field. The absolute pulse energy measurements of ultraviolet light was in the two-color experiments slightly weaker (~ 200 nJ) than in the gas cell and gas jet experiments. However, this was probable due to increased spectral width of the generated light pulses, along with the narrow bandwidth of the mirrors. As seen on figure 5.22 the bandwidth of 3ω light was as high as 50 nm under optimum generation conditions, while the separation mirrors only had high reflectance for 261-266 nm light. Assuming that the generated light has a Gaussian spectral distribution centered around 260 nm with a spectral width of 50 nm, then the width supports deep ultraviolet pulses with durations down to 2 fs. Finally the two-color capillary setup allowed for tunability of the center frequency of the generated ultraviolet light by changing intensity of the generating IR field, as demonstrated in figure 5.21.

6.1 Outlook

The current pulse separation method was mostly implemented as a fast way of removing the fundamental pulses, in order to determine the energy of the ultraviolet pulses. In order to make the setup useful for ultrafast applications a more sophisticated non-dispersive method of pulse separation is needed. One solution is to use the technique of a so-called Brewster reflector[59]. The idea of a Brewster reflector is to place a silicon wafer at Brewster angle for the fundamental frequency², which is therefore coupled into the wafer. Since silicon has a strong absorption resonance in

²Which is 74.9° for 800 nm light.

the visible light, which makes the refractive index very wavelength dependent, the ultraviolet light is instead reflected from the surface. The theoretical reflectance for p polarized 266 nm light at an incidence angle of 74.9° is 0.44, while it is 0.63 for 160 nm light³. In order to avoid diffraction of the pulses from the silicon surface at almost grazing incidence an extremely high surface quality is required.

Another important future perspective of the project would involve a temporal characterization of the pulses. One method of doing this could be based on all vacuum based autocorrelation measurement of the pulse by a pair of D-shaped mirrors as a beam splitter. By mounting one of the mirrors on a piezo-controlled translation stage the delay between the two pulses could be controlled, which would allow for an autocorrelation measurement. In order to measure the autocorrelation between the two pulse an interaction medium is required, this could for example be a gas jet inside a magnetic bottle electron spectrometer, which conveniently exists in the lab. One would then change the delay between the two pulses, and look for an observable effect on the signal from the magnetic bottle electron spectrometer.

Finally the interferometer could probably use an update in order to simultaneous couple the blue and the red light into the fundamental capillary mode. This could for example be achieved by inserting thin focusing lenses in the two arms, and thereby separately focus the beams. An alternative option could be to simply insert an aperture in the blue arm, to reduce the beam size prior to the focusing mirror.

³The reflectance is calculated from the Fresnel equations.

ACKNOWLEDGEMENTS

It has been a great pleasure and a privilege to be part of the Attosecond Physics group at Lund University for the past year. More than anyone, I owe my gratitude to my advisor, Cord Arnold, for providing great guidance and support throughout this project. Also, my initially planned supervisor, Erik Mansten deserves special thanks for his part of the project. I would also like to thank my supervisor at Aarhus University prof. Lars Bojer Madsen for suggesting and providing me with the possibility of visiting Lund University for this project, and for the scientific discussions, although somewhat limited by geography.

Group leader, prof. Anne L’Huillier, deserves heartfelt thanks for accepting me into the group, and treating me as an integral part from day one. By allowing me to not only work on my own project, but also take part in the other activities of the group. Her leading and scientific skills greatly contribute to the very nice atmosphere of the Attosecond group.

Physics can be a very talkative subject with many interesting discussions held, and yet to be had. On this front I would in particular like to thank my current and former office mates: Eleonora Lorek, Diego Guenot, and from the Quantum Information group Adam Wiman and Samuel Tornibue.

I would also like to thank my fellow colleagues in the Attolab, in particular I would like to thank Thomas Fordell and Miguel Miranda for their help and guidance, especially when I first entered the lab.

Any machine requires a well-oiled engine to run smoothly, therefore I would like to thank the administrative team of Atomic Physics: Bertil Hermansson, Camilla Nilsson, Harriett Lindahl and head of division prof. Claes-Göran Wahlström

A warm thanks to all my other colleagues at the Atomic Physics Department, in particular the rest of the members (and former members) of the Attosecond physics group: Johan Mauritsson, Per Johnsson, Mathieu Gisselbrecht, Anders Persson, Fernando Brizuela, Marcus Dahlström, Christoph Heyl, Kathrin Klünder, David Kroon, Linnea Rading, Jörg Schwenke, Deddy Ardiansyah, Rafal Rakowski, Stefanos Carlström, and Piotr Rudawski.

Finally, I would like to thank my friends and family for their support, and encouragement throughout my life, and in particular during the last year.

REFERENCES

- [1] P. A. Franken, A. E. Hill, C. W. Peters, and G. Weinreich. Generation of optical harmonics. *Phys. Rev. Lett.*, 7(4):118–119, Aug 1961.
- [2] T. H. Maiman. Stimulated optical radiation in ruby. *Nature*, 187:493–494, August 1960.
- [3] Claude Rullire *et al.* *Femtosecond Laser Pulses Principles and Experiments 2nd Edition*. Springer, 2003.
- [4] P. B. Corkum. Plasma perspective on strong field multiphoton ionization. *Phys. Rev. Lett.*, 71(13):1994–1997, Sep 1993.
- [5] Anne L’Huillier and Ph. Balcou. High-order harmonic generation in rare gases with a 1-ps 1053-nm laser. *Phys. Rev. Lett.*, 70(6):774–777, Feb 1993.
- [6] P. M. Paul, E. S. Toma, P. Breger, G. Mullot, F. Aug, Ph. Balcou, H. G. Muller, and P. Agostini. Observation of a train of attosecond pulses from high harmonic generation. *Science*, 292(5522):1689–1692, 2001.
- [7] D. Bayer, C. Wiemann, O. Gaier, M. Bauer, and M. Aeschlimann. Time-resolved 2ppe and time-resolved peem as a probe of lsp’s in silver nanoparticles. *Journal of Nanomaterials*, 2008:1–12, 2008.
- [8] Siegfried Lnnemann, Alexander I. Kuleff, and Lorenz S. Cederbaum. Ultrafast charge migration in 2-phenylethyl-n,n-dimethylamine. *Chemical Physics Letters*, 450(4-6):232 – 235, 2008.
- [9] F. Remacle, M. Nest, and R. D. Levine. Laser steered ultrafast quantum dynamics of electrons in lih. *Phys. Rev. Lett.*, 99(18):183902, Nov 2007.
- [10] Florentin Reiter, Ulrich Graf, Martin Schultze, Wolfgang Schweinberger, Hartmut Schröder, Nicholas Karpowicz, Abdallah Mohammed Azzeer, Reinhard Kienberger, Ferenc Krausz, and Eleftherios Goulielmakis. Generation of sub-3 fs pulses in the deep ultraviolet. *Opt. Lett.*, 35(13):2248–2250, Jul 2010.
- [11] L. Misoguti, S. Backus, C. G. Durfee, R. Bartels, M. M. Murnane, and H. C. Kapteyn. Generation of broadband vuv light using third-order cascaded processes. *Phys. Rev. Lett.*, 87(1):013601, Jun 2001.
- [12] F. Seifert, J. Ringling, F. Noack, V. Petrov, and O. Kittelmann. Generation of tunable femtosecond pulses to as low as 172.7 nm by sum-frequency mixing in lithium triborate. *Opt. Lett.*, 19(19):1538–1540, Oct 1994.

- [13] A. Borsutzky, R. Brnger, and R. Wallenstein. Tunable uv radiation at short wavelengths (188240 nm) generated by sum-frequency mixing in lithium borate. *Appl. Phys. B*, pages 380–384, 1991.
- [14] David J. Griffiths. *Introduction to Electrodynamics 3rd Edition*. Prentice-Hall, 1999.
- [15] Peter W. Milonni and Joseph H. Eberly. *Lasers*. John Wiley and Sons, Inc, 1988.
- [16] Robert W. Boyd. *Nonlinear Optics 3rd Edition*. Academic Press, 2008.
- [17] M. Bass, P. A. Franken, J. F. Ward, and G. Weinreich. Optical rectification. *Phys. Rev. Lett.*, 9(11):446–448, Dec 1962.
- [18] A. E. Siegman. *Lasers*. University Science, Mill Valley, 1986.
- [19] Simin Feng and Herbert G. Winful. Physical origin of the gouy phase shift. *Opt. Lett.*, 26(8):485–487, Apr 2001.
- [20] L. M. Pedrotti F. Pedrotti and L. S. Pedrotti. *Introduction to Optics 3rd Edition*. Pearson Education, 2007.
- [21] G. Bjorklund. Effects of focusing on third-order nonlinear processes in isotropic media. *Quantum Electronics, IEEE Journal of*, 11(6):287 – 296, June 1975.
- [22] J. J. Sakurai. *Modern Quantum Mechanics Revised Edition*. Addison-Wesley, 1994.
- [23] R. Miles and S. Harris. Optical third-harmonic generation in alkali metal vapors. *Quantum Electronics, IEEE Journal of*, 9(4):470 – 484, April 1973.
- [24] H.J. Lehmeier, W. Leupacher, and A. Penzkofer. Nonresonant third order hyperpolarizability of rare gases and n2 determined by third harmonic generation. *Optics Communications*, 56(1):67 – 72, 1985.
- [25] B. H. Bransden and C. J. Joachain. *Physics of Atoms and Molecules 2nd Edition*. Pearson Education, 2003.
- [26] Bahaa E. Salah and Malvin Carl. *Fundamentals of Photonics 2nd Edition*. Wiley and Sons, 2007.
- [27] Marvin J. Weber (ed.). *Handbook of Optical Materials*. CRC Press, 2003.
- [28] Richard Syms and John Cozens. *Optical Guided Waves and Devices*. McGraw-Hill Companies, 1992.
- [29] R. Paschotta (ed.). *Encyclopedia of Laser Physics and Technology*. RP Photonics Consulting GmbH, Internet Version 2011.
- [30] Mitsunobu Miyagi and Shigeo Nishida. Pulse spreading in a single-mode fiber due to third-order dispersion. *Appl. Opt.*, 18(5):678–682, Mar 1979.
- [31] Richard P. Feynman. *The Feynman Lectures on Physics Vol. 2*. Addison-Wesley, 1964.

-
- [32] A. Couairon and A. Mysyrowicz. Femtosecond filamentation in transparent media. *Physics Reports*, 441(2-4):47 – 189, 2007.
- [33] A. E. J. Marcatili and R. A. Schmeltzer. Hollow metallic and dielectric waveguides for long distance optical transmission and lasers. *The bell system technical journal*, 43(4), July 1964.
- [34] J. A. Stratton. *Electromagnetic Theory*. McGraw-Hill Book Company, 1941.
- [35] P. Chernev and V. Petrov. Self-focusing of light pulses in the presence of normal group-velocity dispersion. *Opt. Lett.*, 17(3):172–174, Feb 1992.
- [36] M. Kolesik, J. V. Moloney, and M. Mlejnek. Unidirectional optical pulse propagation equation. *Phys. Rev. Lett.*, 89(28):283902, Dec 2002.
- [37] C L Arnold, B Zhou, S Akturk, S Chen, A Couairon, and A Mysyrowicz. Pulse compression with planar hollow waveguides: a pathway towards relativistic intensity with table-top lasers. *New Journal of Physics*, 12(7):073015, 2010.
- [38] T. Fordell, M. Miranda, A. Persson, and A. L’Huillier. Carrier-envelope phase stabilization of a multi-millijoule, regenerative-amplifier-based chirped-pulse amplifier system. *Opt. Express*, 17(23):21091–21097, Nov 2009.
- [39] R Szipocs, K Ferencz, C Spielmann, and F Krausz. Chirped multilayer coatings for broadband dispersion control in femtosecond lasers. *Optics Letters*, 19(3):201, 1994.
- [40] Steven T Cundiff. Phase stabilization of ultrashort optical pulses. *Journal of Physics D: Applied Physics*, 35(8):R43, 2002.
- [41] Takao Fuji, Jens Rauschenberger, Christoph Gohle, Alexander Apolonski, Thomas Udem, Vladislav S Yakovlev, Gabriel Tempea, Theodor W Hnsch, and Ferenc Krausz. Attosecond control of optical waveforms. *New Journal of Physics*, 7(1):116, 2005.
- [42] M. D. Perry, F. G. Patterson, and J. Weston. Spectral shaping in chirped-pulse amplification. *Opt. Lett.*, 15(7):381–383, Apr 1990.
- [43] M. Swoboda, T. Fordell, K. Klünder, J. M. Dahlström, M. Miranda, C. Buth, K. J. Schafer, J. Mauritsson, A. L’Huillier, and M. Gisselbrecht. Phase measurement of resonant two-photon ionization in helium. *Phys. Rev. Lett.*, 104(10):103003, Mar 2010.
- [44] Alpha-1000 us/a instruction manual.
- [45] G. Cheriaux, P. Rousseau, F. Salin, J. P. Chambaret, Barry Walker, and L. F. Dimauro. Aberration-free stretcher design for ultrashort-pulse amplification. *Opt. Lett.*, 21(6):414–416, Mar 1996.
- [46] D.C. Brown. The promise of cryogenic solid-state lasers. *Selected Topics in Quantum Electronics, IEEE Journal of*, 11(3):587 – 599, may-june 2005.
- [47] Michele Giunta. *Master Thesis: Laser beam pointing and power stabilization by fast feedback loop control*. Lund University, 2011.

- [48] M. D. Perry, T. Ditmire, and B. C. Stuart. Self-phase modulation in chirped-pulse amplification. *Opt. Lett.*, 19(24):2149–2151, Dec 1994.
- [49] Masahiko Daimon and Akira Masumura. High-accuracy measurements of the refractive index and its temperature coefficient of calcium fluoride in a wide wavelength range from 138 to 2326 nm. *Appl. Opt.*, 41(25):5275–5281, Sep 2002.
- [50] Gorachand Ghosh. Dispersion-equation coefficients for the refractive index and birefringence of calcite and quartz crystals. *Optics Communications*, 163(1-3):95 – 102, 1999.
- [51] John H. Burnett, Zachary H. Levine, and Eric L. Shirley. Intrinsic birefringence in calcium fluoride and barium fluoride. *Phys. Rev. B*, 64(24):241102, Nov 2001.
- [52] D. Proch and T. Trickl. A high-intensity multi-purpose piezoelectric pulsed molecular beam source. *Rev. Sci. Instrum.*, 60(4):713–716, 1989.
- [53] P. Karlitschek, G. Hillrichs, and K. F. Klein. Photodegradation and nonlinear effects in optical fibers induced by pulsed uv-laser radiation. *Optics Communications*, 116(1-3):219 – 230, 1995.
- [54] P. W. Dooley, I. V. Litvinyuk, Kevin F. Lee, D. M. Rayner, M. Spanner, D. M. Villeneuve, and P. B. Corkum. Direct imaging of rotational wave-packet dynamics of diatomic molecules. *Phys. Rev. A*, 68(2):023406, Aug 2003.
- [55] S.G Jennings. The mean free path in air. *Journal of Aerosol Science*, 19(2):159 – 166, 1988.
- [56] M. Nisoli, S. De Silvestri, and O. Svelto. Generation of high energy 10 fs pulses by a new pulse compression technique. *Applied Physics Letters*, 68(20):2793 –2795, may 1996.
- [57] M. Nisoli, G. Sansone, S. Stagira, C. Vozzi, S. De Silvestri, and O. Svelto. Ultra-broadband continuum generation by hollow-fiber cascading. *Applied Physics B: Lasers and Optics*, 75:601–604, 2002.
- [58] K. Klünder, J. M. Dahlström, M. Gisselbrecht, T. Fordell, M. Swoboda, D. Guénot, P. Johnsson, J. Caillat, J. Mauritsson, A. Maquet, R. Taïeb, and A. L’Huillier. Probing single-photon ionization on the attosecond time scale. *Phys. Rev. Lett.*, 106(14):143002, Apr 2011.
- [59] Eiji J. Takahashi, Hirokazu Hasegawa, Yasuo Nabekawa, and Katsumi Midorikawa. High-throughput, high-damage-threshold broadband beam splitter for high-order harmonics in the extreme-ultraviolet region. *Opt. Lett.*, 29(5):507–509, Mar 2004.